

Model catalytic oxide surfaces: a study of the $\text{LaAlO}_3(001)$ surface



James M Rondinelli

Advisers

Professor Laurence D Marks

Courtney H Lanier

Department of Materials Science and Engineering

Northwestern University

Evanston, Illinois USA

June 2006

Submitted in partial fulfillment of the requirements of the degree of

Bachelor of Science with Honours

© Copyright 2006 by James M Rondinelli
All Rights Reserved

The aspects of things that are most important for us are hidden because of their simplicity and familiarity. (One is unable to notice something—because it is always before one's eyes.) . . . And this means: we fail to be struck by what, once seen, is most striking and most powerful.

—Ludwig Wittgenstein*

*from Ludwig Wittgenstein's *Philosophical Investigations*, trans. G.E.M. Anscombe, 3rd ed. (New York, 1958), sect. 129, p.50e.

Acknowledgements

First, I would like to thank my thesis adviser, Professor L.D. Marks for allowing a sophomore in the spring of 2004, the opportunity to participate in academic research. Since then, his continued support and encouragement for my work has been an inspiration to me. I am also indebted to Courtney Lanier, a graduate student in the Marks group who has spent countless hours working along side me on this project, and has acted as a second adviser. I would also like to thank Professor K.R. Poeppelmeier for his stimulating conversations, and maintaining his chemical intuition throughout this project. Dr. Kathleen Stair, also reviewed much of this work, and has served as a great teacher and mentor. Her advice on making complex ideas readily available for general discussions has been extremely helpful.

I would also like to thank past and present members of the Marks group—Dr. Ann Chiamonti Debay, Dr. Arun Subramanian, Dr. Chris Own, Dr. Bin Deng, Dr. Yingmin Wang, Arno Merkle, Brian Quezada, Robin Koshy, and Jim Ciston—for many memorable experiences in and out of the laboratory. These individuals have not only shared their own expertise, but have also allowed me to collaborate on many of their own projects. Without their helpful discussions and light-hearted spirit, this project would not have been as successful.

I am also thankful to all of my friends, not only in the Materials Department, but those I have met while at Northwestern. These are the individuals who have kept life interesting the past few years. For our successes are built upon these everyday, ordinary experiences and relationships. These are the relationships not found solely with parents, family and faculty; but more, the relationships with each other. For these friends I am truly grateful.

This work was funded by the National Science Foundation, Northwestern University, Institute for Environmental Catalysis, and the Institute for Catalysis in Energy Processes in collaboration with the Materials Research Science and Engineering Center. An Undergraduate Research Grant from the Office of the Provost allowed for the purchase of many of the materials in this study. Much of the experimental work was performed in the EPIC facility of NUANCE Center at Northwestern University. NUANCE Center is supported by NSF-NSEC, NSF-MRSEC, Keck Foundation, the State of Illinois, and Northwestern University.

Abstract

Insight into the nature of surfaces and the processes which occur on them is of great importance in the study of catalysis. For example, mixed metal oxides are known to be catalytically active for the oxidation of CO and the reduction of NO_x (automobile exhaust). A practical example of the need for better catalysts is in the chemical industry, where approximately 50% of the total municipal solid waste generated annually is in the form of by-product waste; this amounts to more than 100 million tons annually. The prerequisite of understanding the atomic scale structure at surfaces is what enables the engineering of new and more efficient materials. Through these studies catalytically active sites and reaction pathways may be explored in order to improve the activity and selectivity of catalytic oxidation.

This work focuses on understanding the surface structures of catalytic oxide materials. A low-index face of a model perovskite material, lanthanum aluminate, is investigated through transmission electron diffraction and imaging techniques. The approach taken is to recrystallize the surface through air anneal treatments in an attempt to stabilize different reconstructions. In this study, the discovery of the $(\sqrt{5} \times \sqrt{5})R26.6^\circ$ reconstruction on the LaAlO₃ (001) surface at temperatures between 1100°C - 1500°C is reported. Surface structure analysis is performed with Direct Methods to obtain plausible scattering potential maps, from which the surface unit cell contents can be determined. It is shown that the surface exhibits faceting along the $\langle 100 \rangle$ direction and subsurface voids. Furthermore, an oxygen rich surface containing lanthanum vacancies is shown to be responsible for the surface reconstruction. Density functional theory (DFT) calculations have been performed on the surface, which suggest that an electron hole is localized near the

first one or two surface layers. This charge defect provides the necessary charge balance at the interface. Finally, consequences of the electronic structure redistribution are discussed; as they are likely to be applicable to other oxides and perovskite materials.

Contents

1	Introduction	1
1.1	Surface Dynamics and Reconstructions	4
2	Characterization Techniques and Experimental Procedures	6
2.1	Transmission Electron Microscopy	6
2.1.1	Forming Diffraction Patterns and Images	8
2.1.2	Crystal Diffraction	10
2.1.2.1	Bragg's Law	12
2.1.2.2	The Ewald Sphere Construction	14
2.1.2.3	Selected Area Diffraction	17
2.1.3	Image Formation	17
2.1.3.1	Diffraction Contrast	18
2.1.3.2	Phase Contrast	19
2.1.3.3	Bright and Dark Field Images	19
2.2	Sample Preparation	20
2.3	Obtaining Surface Specific Information	21
2.3.1	Diffraction Analysis	22
2.4	The Crystallographic Phase Problem	23
2.4.1	Electron Direct Methods	24
3	Reconstructions on the LaAlO₃ (001) Surface	28
3.1	Background	28
3.1.1	The Perovskite Crystal Structure	28
3.1.2	Polar Surfaces	30
3.1.3	Previous Surface Studies	32
3.2	TEM Surface Studies	36
3.2.1	Disordered Surface	36
3.2.2	Recrystallized Surface	38
3.2.3	Reconstructed Surface	38

3.3	Structure Completion and Refinement	42
3.3.1	Bulk Registry	47
3.3.2	Solution to the $(\sqrt{5} \times \sqrt{5})R26.6^\circ$ Surface	50
3.3.2.1	Structural Refinement	50
3.3.2.2	Charge Analysis	51
4	Conclusions and Suggestions for Future Work	57
	References	65

List of Figures

1.1	The first three layers of the face centered cubic (110) surface are shown with the respective primitive unit cells designated by dashed lines: (a) no reconstruction, (b) missing row reconstruction. The large circles indicate atoms at the surface, gray circles one layer down, and solid circles indicate atoms two layers down.	5
2.1	Schematic diagram of the principle components of a transmission electron microscope.	8
2.2	Schematic ray diagrams of (a) the formation of a diffraction pattern in the back focal plane of the objective lens, (b) the position of the objective aperture to form a bright field image, and (c) dark field image formed by tilted incident illumination.	9
2.3	Schematic diagrams of monochromatic diffraction of light by a line grating with slit width a	11
2.4	(a) Schematic illustration of Bragg reflection in a crystal at an angle Θ from two crystal planes, and (b) the relationship of the incident, transmitted and diffracted beams in transmission geometry.	13
2.5	Reciprocal space vector diagram describing the reflection by a set of (hkl) planes.	14
2.6	Ewald sphere construction for a reciprocal lattice point (hkl) showing how the intensity of a diffracted beam deviates from the ideal Bragg condition.	15
2.7	The Ewald sphere construction in reciprocal space shown schematically with the specimen, transmitted and diffracted beams, along with the resultant diffraction pattern.	16

LIST OF FIGURES

- 3.1 The ideal ABX_3 cubic perovskite structure illustrating the octahedral coordination of the B-site (aluminum here) cations (for $LaAlO_3$). 28
- 3.2 The low temperature $LaAlO_3$ rhombohedral unit cell (outlined in green) is shown relative to the cubic perovskite (outlined in black). NB.: bulk LAO contains two formula units at room temperature. 29
- 3.3 The three types of atomic configurations are shown, with the repeat unit bracketed: **(a)** Type I, equal number of cations and anions per atomic plane; **(b)** Type II, charged plane without a net dipole moment; **(c)** charged planes with a net dipole moment perpendicular to the surface. 31
- 3.4 Alternating planes of LaO and AlO_2 are shown stacking in the $\langle 001 \rangle$ cubic direction. Simple electron counting models show that bulk termination leads to a polar surface requiring a charge compensating mechanism at the surface-vacuum interface. . . . 32
- 3.5 Dark-field TEM image of the $LaAlO_3(001)$ surface following the ion-milling process showing bend contours which suggests a stressed sample. 37
- 3.6 An on-zone $LaAlO_3(001)$ selected-area diffraction (SAD) pattern is shown prior to annealing treatments. NB.: the pattern is indexed to the rhombohedral unit cell, $[11\bar{1}]$ zone. 37
- 3.7 An off-zone SAD of the $LaAlO_3(001)$ surface prior to annealing and following Ar^+ ion bombardment. The diffuse ring around the bulk (1×1) spots is indicative of a disordered surface. . . . 38
- 3.8 Annealing of the $LaAlO_3(001)$ surface at $800^\circ C$ for 3 hours results in a recrystallized surface as illustrated by the absence of the diffuse ring in this off-zone SAD pattern. At this temperature no reconstruction is observed. The (1×1) bulk terminated rhombohedral surface unit cell is outlined. 39
- 3.9 Dark field image of the $LAO(001)$ surface after a 3 hour anneal at $800^\circ C$. Preliminary faceting is visible in the image. As the anneal time increases larger facets with fewer defects result. . . 39

-
- 3.10 Annealing of LaAlO₃ (001) over the range of 1100°C to 1500°C for 3 hours results in a $(\sqrt{5} \times \sqrt{5})R26.6^\circ$ surface reconstruction with respect to the rhombohedral bulk unit cell. A focused probe off-zone diffraction pattern is shown with the rhombohedral (1×1) bulk unit cell (orange) and the surface unit cell for both domains of the reconstruction (green). 40
- 3.11 Dark field image of the $(\sqrt{5} \times \sqrt{5})R26.6^\circ$ surface on LAO after a 3 hour anneal (1100°C). The formation of $\langle 100 \rangle$ facets, with respect to the cubic face, occur at this temperature and can be seen in the image. Small rectangular features are discernible near the edge of the sample. These features do not show any strain contrast in the image which suggests they are not particles or trapped gas. Similar voids have been observed on other perovskite materials, like SrTiO₃. This reconstruction is extremely reproducible and has been shown to be air stable for several months. 41
- 3.12 High resolution image of the LAO(001) surface after a 3 hour anneal at 1100°C. Faceting is visible along the edge and several voids are present throughout the sample. 42
- 3.13 Surface diffraction pattern for the $(\sqrt{5} \times \sqrt{5})R26.6^\circ$ reconstruction. The annulus outlined in the diffraction pattern contains the reflections used in Direct Methods. The remaining reflections were removed from the data set. Circles are drawn at 0.25 and 0.80 Å⁻¹. 43
- 3.14 Direct Methods scattering potential map for **(a)** the LaAlO₃ $(\sqrt{5} \times \sqrt{5})R26.6^\circ$ reconstructed surface, and **(b)** the Babinet solution, with the non-primitive surface unit cell ($a=11.978 \text{ \AA}$, $\alpha = 89.89^\circ$) drawn in (white). Regions of high potential in this projected scattering map correspond to likely locations for atoms. 45
- 3.15 Structure solution map following refinements. The surface model has been overlaid. The bright spots correspond to La atoms (violet) and the weaker spots correspond to O atoms (cyan). The non-primitive surface unit cell ($a=11.978 \text{ \AA}$, $\alpha = 89.89^\circ$) has also been drawn in (white). The orientation of the bulk relative to the surface reconstruction is denoted by the [100] and [010] axes (green). 46

-
- 3.16 Bulk layers of **(a)** LaO and **(b)** AlO₂ with respect to the non-primitive surface unit cell ($a=11.978 \text{ \AA}$, $\alpha = 89.89^\circ$), with oxygen atoms at the origin (cyan) and lanthanum (violet) or aluminum (red) atoms, respectively. 47
- 3.17 The $(\sqrt{5} \times \sqrt{5})R26.6^\circ$ structure solution from Direct Methods, the z-height positions are determined from typical bulk values and bond constraints. The La vacancy is discernible at the surface layer. The atoms are denoted as follows: oxygen (cyan), aluminum (red) and lanthanum (violet). 49
- 3.18 DFT solution of the $(\sqrt{5} \times \sqrt{5})R26.6^\circ$ surface structure: **(a)** top view with the surface unit cell outlined in black ($a=8.537 \text{ \AA}$, $\alpha = 90.00^\circ$), and **(b)** sideview. Atoms O1, O2 (blue) and La3 (magenta) are in the surface layer, while Al4, O6, O7 and O8 are in the second layer. 52
- 3.19 DFT solution of the $(\sqrt{5} \times \sqrt{5})R26.6^\circ$ surface structure: **(a)** sideview, and **(b)** top view with the surface unit cell outlined in black ($a=8.537 \text{ \AA}$, $\alpha = 90.00^\circ$). The AlO₆ octahedra have been shaded and the large distortion in the first surface layer is apparent. Surface lanthanum atoms are colored magenta, and surface oxygen atoms are blue. 54

List of Tables

3.1	Summary of observed surface terminations (or reconstructions) on the LaAlO_3 (001) surface.	34
3.2	Experimental and DFT atom positions for the $(\sqrt{5} \times \sqrt{5})R26.6^\circ$ reconstruction.	53
3.3	Bader's AIM analysis of the partial atomic charges for the surface atoms of the $(\sqrt{5} \times \sqrt{5})R26.6^\circ$ surface reconstruction.	55

CHAPTER 1

Introduction

God created the solid state, but surfaces were the work of the Devil.

W.E. PAULI

I begin this thesis with a quote by Wolfgang Pauli, who upon recognizing the complexity of the physical phenomenon occurring on solid surfaces, declared that the *surface* must be the invention of the devil. It is my intention that this work dismisses some of these apprehensions for other students embarking on similar studies and contributes to the ever-growing body of literature on surface structure dynamics. Additionally, it has been my experience that the surfaces of materials are often dismissed in an undergraduate materials science curriculum and emphasis is placed on bulk materials properties. While this may be the best approach at the moment for cultivating a deep understanding into the physics of materials, it is at this interface, the *surface*, where the richness of materials science is truly manifest.

Until the invention of the electron microscope it was not possible to probe the basic nature of matter. While optical microscopes have been around for centuries, it is the consequence of the wave nature of light—in particular its wavelength (of about half a micron)—that had prevented the study of the structure of materials at smaller length scales. Today, the atomic structure of bulk materials and the instruments to investigate them are becoming increasingly commonplace. However, as the processing and engineering of novel nanomaterials becomes evermore routine, an advance physical understanding of the structure and dynamics of atomic scale surfaces is necessary. We can no longer avoid the question of what is going on at the surface. With the miniaturization of materials, the ratio of surface to bulk atoms approaches unity and quantum mechanical effects are observed. Since macroscopic properties

of such solid materials are attributable to the atomic scale structure at crystalline surfaces, developing a capable intuition of this interface is paramount in order to cleverly design new materials with anticipated properties.

A common problem with surface structure investigations is that bulk thermodynamic arguments fail at predicting the structure at this interface. The inability to successfully make such determinations *a priori* has resulted in the creation of an entire experimental field devoted to exploring such issues. While much work has been done on understanding the atomic structure of surfaces on metals, knowledge of transition metal oxide surfaces is minimal. The richness of these materials is attributed to the ability of the cations in the lattice to change oxidation state and coordination at the surface. An investigation of these material systems is therefore required because they are typically used for heterogeneous catalysis—a field of which is of particular interest in this work.

Insight into the nature of surfaces and the processes which occur on them is of great importance in the study of catalysis. These catalytic materials are routinely used for the oxidative dehydrogenation of butane and propane into *greener* products. It is within this field that the broader impact of surface science studies of mixed metal oxides becomes clear. For example, approximately 50% of the total municipal solid waste generated annually in the United States is attributed to the chemical industry in the form of by-product waste. This amounts to more than 100 million tons annually [1].

The goal of this research is to improve the activity and selectivity of catalytic oxidation by identifying catalytically active sites and reaction pathways through atomic scale structure analysis. It is these important prerequisites that will make the engineering of new and more efficient materials possible. The ramifications of this work may result in positive environmental impacts on various industrial activities, including chemical production and fossil fuel consumption.

In the present work, we chose to study the surface structure of a simple model catalytic oxide, with the aim of providing a structure–reactivity relationship for heterogeneous catalysis. Historically, developments in the field of heterogeneous catalysis have been made through Edisonian techniques, namely trial and error. However, researchers are beginning to offer insight into the underlying processes of catalysis in hopes of determining accurate reaction pathways [2]. By definition a catalyst reduces the free energy barrier required

for a reaction to reach an equilibrium state without actually being consumed in the reaction itself.

Moreover, heterogeneous catalysis is inherently selective, in that it is site-specific and structurally dependent. In order to understand such catalytic reactions and identify catalytically active sites, knowledge of the atomic scale structure of the surface is required. A classic example of the structure–reactivity relationship was shown by Bozso *et al.* for the synthesis of ammonia [3]. They found that the synthesis rate varied by a couple of orders of magnitude on the different faces ((001), (110) and (111)) of iron. A caveat worth noting is that examination of industrial oxide catalysts is complicated by the fact that they are high surface area powders (and used at high pressures), which hinders the ability to determine active sites. While we recognize these facts, studies of this sort are required to elucidate how physical phenomenon, i.e. valence and coordination transitions at the surface contribute to the activity and selectivity of the material. For this reason, high quality single crystals of known crystallographic orientation are examined. In particular we investigate the (001) surface of Lanthanum Aluminate (LaAlO_3 , LAO).

Routine characterization techniques for investigating the atomic scale crystal structure of surfaces in real space include scanning tunneling microscopy (STM), transmission electron microscopy (TEM) with the associated high-resolution electron microscopy (HREM) and scanning transmission electron microscopy (STEM) approaches. Some diffraction techniques such as grazing incidence X-ray diffraction (GIXD), transmission electron diffraction (TED), low-energy electron diffraction (LEED) and reflection high-energy electron diffraction (RHEED) also provide Fourier space information about a material [4–7].

The approach taken in this work to stabilize different surface reconstructions on a low index face (001) by high temperature annealing treatments at various dwell times, temperatures and pressures. The primary tools used to study surface reconstructions in this work are TEM/TED techniques complemented with various spectroscopic techniques to determine chemical composition and electronic structure. Such instruments include x-ray photoelectron spectroscopy (XPS) and auger electron spectroscopy (AES). Although low signal levels are recorded in transmission geometry for electron diffraction due to bulk attenuation, it has the advantage of simultaneously providing both real and reciprocal space information at various length scales of the surface structure. While diffraction appears to be a rather simple technique it has been

1.1 Surface Dynamics and Reconstructions

shown to be a powerful instrument for surface crystallographers. Since the periodicity of a surface structure is different than the bulk, weak additional superstructure spots result in TED patterns. To that end, the atomic structure of a surface can be investigated through a combination of electron diffraction and Direct Methods (DM).

Included in this introduction is a brief review of fundamental surface dynamics theory. The details of the experimental procedures and characterization methodology will be discussed in Chapter 2, and the results obtained in this work in Chapter 3. The latter will focus on the possible mechanisms which may provide for charge compensation at the surface. Similarly, a discussion of the reported surfaces terminations by various research groups are examined, and the discrepancies among them are shown to motivate the current study. This thesis concludes with a summary and suggestions for future work (Chapter 4).

1.1 Surface Dynamics and Reconstructions

For this work, we define a *surface* as the boundary between a bulk solid and its environment [8]. Termination of a crystal results in the creation of surfaces which effectively modify the atomic arrangement of atoms at the near the surface region. Two phenomena are seen with bulk truncation: (1) relaxation where the distance between atomic planes in the direction parallel to the surface deviate from typical bulk values, and (2) surface reconstruction where lateral structural alteration allows for atomic rearrangements on the surface plane [9]. The surface *reconstructs* into a phase with new symmetry which can occur either spontaneously or be activated by thermal excitation or adsorbates.

Typically atoms located within the bulk experience an electrostatic attraction from the atoms completely surrounding them. However, atoms at the surface are only subjected to an inward attraction by bulk atoms. The new charge distribution induces electrostatic forces on the ion cores which effectively contracts the first interlayer spacing (this is the relaxation effect) [10]. In other words, the bulk periodicity is interrupted at the surface along a specified direction and leads to a loss of coordination or “dangling bonds”. Consequently, the surface layers have a higher energy than those in the bulk and this excess energy (or surface free energy) creates a driving force for structural rearrangement.

1.1 Surface Dynamics and Reconstructions

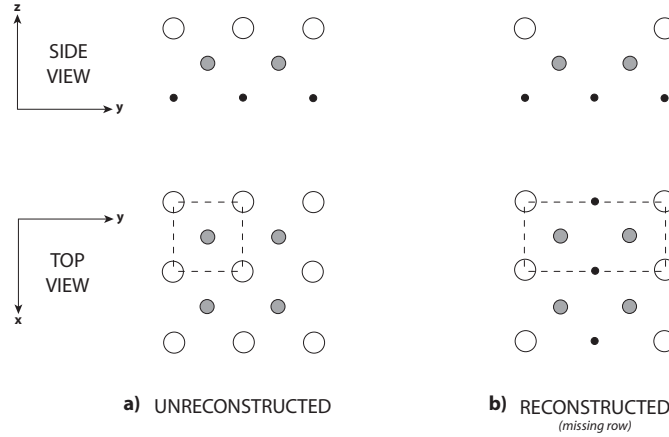


Figure 1.1: The first three layers of the face centered cubic (110) surface are shown with the respective primitive unit cells designated by dashed lines: **(a)** no reconstruction, **(b)** missing row reconstruction. The large circles indicate atoms at the surface, gray circles one layer down, and solid circles indicate atoms two layers down.

When surfaces are subjected to the appropriate environmental conditions, the atoms will organize into structures that demonstrate periodicities larger than the bulk. Such behavior is clearly evident on low index surfaces, such as the (001) orientation, as examined in this work, due to the high density of dangling bonds. Typically a few atomic layers participate in the surface reconstruction and consequently introduce new strain fields into the material. Surface structures are then classified by one of the 17 crystallographic plane groups since such structures demonstrate only two-dimensional periodicity (Fig. 1.1). The reconstruction is then described in terms of size and orientation relative to the primitive (1×1) bulk lattice [11].

CHAPTER 2

Characterization Techniques and Experimental Procedures

2.1 Transmission Electron Microscopy

Historically, transmission electron microscopy (TEM) has been a complementary tool for X-ray structural crystallographers owing to the insufficient image resolution at the time (which as of now has been overcome) and in the poor quality of diffraction data, as a consequence of multiple (dynamical) scattering. Today however, the electron microscope has the advantage of being able to form a fine probe for nanoscale characterization, while simultaneously allowing for the collection of improved diffraction patterns with kinematical or near-kinematical data. TEM allows for a variety of materials characterization experiments on not only bulk materials properties, but surface information can also be obtained. For example, surface morphology, surface unit cell dimensions, surface atomic positions, and even surface charge density and charge transfer can be observed [11–15]. One of the most well known examples of the surface sensitivity of TEM include the solution to the Si(111)- 7×7 DAS surface structure by Takayanagi *et al.* [16, 17].

With the development of new aberration-corrected lenses in the electron microscope, high-resolution imaging (HREM) has been able to achieve resolutions on the order of a few angstroms [18]. However, electron diffraction still remains the most powerful technique for extracting structural information with higher resolutions (sub-picometer) since diffraction is not limited by the aberrations of the objective lens (as is the case for imaging). While high resolution real space imaging provides some atomic scale information, it is insufficient at providing the necessary surface information for determining surface structures. The diffraction data although still suffers from the classic *phase problem* that X-ray crystallographers experienced in the 1950s [19]. Since the phases of diffracted beams are lost in a TEM experiment, and only intensities

2.1 Transmission Electron Microscopy

are measured, phase relationships must be recovered to solve the structure directly. Direct Methods (DM) provides the solution to this well known *phase problem* in crystallography and diffraction. If both phase and amplitude of the diffracted beams were known, the structure factor would be completely described and linear Fourier analysis would produce straightforward structure models. A more thorough review of DM is given in Sec. 2.4.1.

Before describing the TEM investigation approach, I will briefly explain how the TEM operates. A full analysis of image formation (including contrast) and interpretation requires dynamical scattering theory, but a more simpler approach invokes single scattering (kinematical) theory. It is important to note that while kinematical theory is useful for describing many qualitative results, it is only accurate in specific cases, i.e. when scattering is essentially incoherent. While I will not develop this single scattering theory completely, I will use some of its results throughout the analysis. For a complete review of both kinematical and dynamical scattering theory I refer you to the literature [20–22].

In essence, the electron microscope acts similar to a slide projector, in that rather than passing light through a piece of film to generate an image; electrons are passed through a thin sample. The microscope uses a series of magnetic lenses, while accelerating the electrons through a high potential in vacuum, to focus an electron beam onto a sample. The main components of the microscope are shown in Fig. 2.1. The Hitachi microscope used in these surface studies uses a resistively heated tungsten filament, mounted on a ceramic material, that rests behind a Wehnelt cover with a hole at the center. The Wehnelt is set at a negative potential to ensure that only thermionic emitted electrons ejected near the very center of filament tip form the electron probe. The electron probe which leaves the tungsten tip is usually on the order of several microns. For this reason, the electrons are focused (and accelerated) by a condenser lens system on to the sample, while apertures limit the solid angle of the electron probe. These lenses demagnify the beam by about 50X, such that its diameter is less than a micron.

Since electrons can be described as complex plane waves, when they interact with the sample, some of the incident waves will pass directly through the sample (inelastic scattering) while others will be diffracted (elastic scattering). As the electrons exit the sample, they are focused by the objective lens at the back focal plane to form the diffraction pattern. They then pass through

2.1 Transmission Electron Microscopy

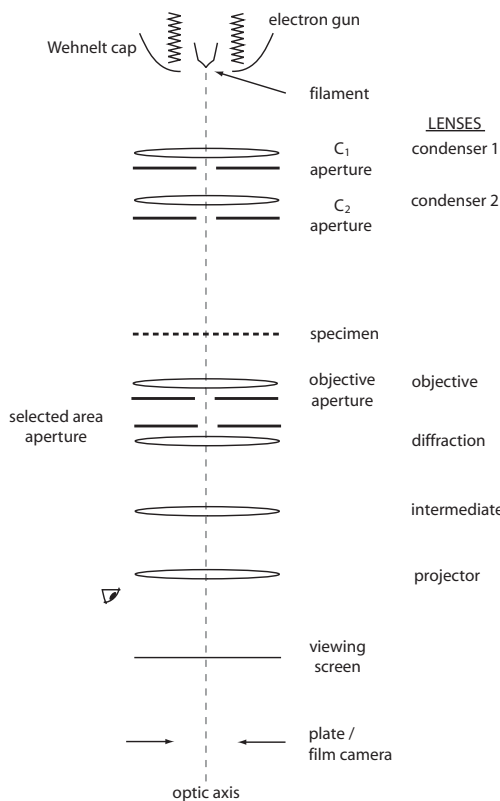


Figure 2.1: Schematic diagram of the principle components of a transmission electron microscope.

the focal point of the lens to the image plane of the objective lens where the electrons form the image. Image contrast may be enhanced with the use of an objective aperture—inserted at the focal plane of the lens—and the area from which diffraction information is collected can be controlled by using a selected area aperture. The different imaging planes are one of the microscope's greatest strengths as a characterization tool, in that it enables the collection of real or reciprocal space information. Magnification is controlled by the excitation of intermediate lens (a four-lens system is shown in Fig. 2.1) and the image or diffraction pattern is visible on a phosphor screen. A camera or film below the screen may be used to record images.

2.1.1 Forming Diffraction Patterns and Images

As noted, a TEM can produce both diffraction patterns and several types of images, all of which have been used in this surface study. The typical investigation requires a combination of these two types of information and correlating their results to make definitive conclusions. The purpose of this section is

2.1 Transmission Electron Microscopy

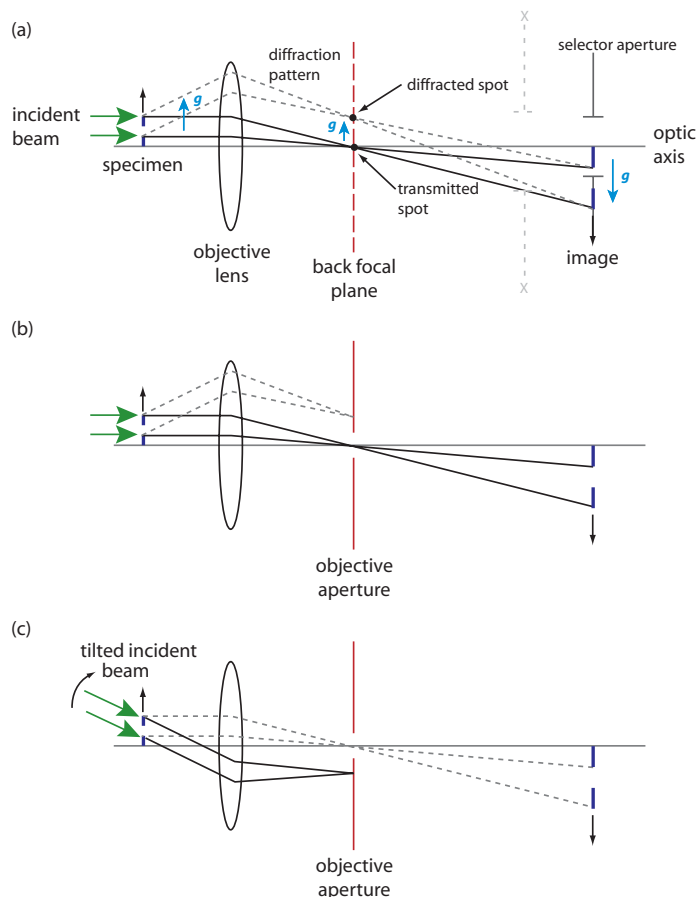


Figure 2.2: Schematic ray diagrams of (a) the formation of a diffraction pattern in the back focal plane of the objective lens, (b) the position of the objective aperture to form a bright field image, and (c) dark field image formed by tilted incident illumination.

to briefly explain how the different images are formed in the microscope. The simplest approach to understanding the different operation modes is through classic ray diagrams. Fig. 2.2a shows a parallel illumination source (along the optic axis) impinging on a specimen. As the image is formed the transmitted beam (solid line) and diffracted beam (dashed line) are focused onto the back focal plane of the objective lens. It is here, where the diffraction pattern is formed. As can be seen from Fig. 2.2a both the diffraction pattern and image are simultaneously produced, and the microscopist can select which of these two are brought into focus on the viewing screen with the remaining magnification lens system.

2.1 Transmission Electron Microscopy

2.1.2 Crystal Diffraction

Electrons can be described as particle waves with a characteristic wavelength, λ , given by the de Broglie relation, $mv = h\lambda$. For a particular accelerating voltage, V_c , the relativistically corrected wavelength is

$$\lambda = \frac{h}{[2mV_c e(1 + eV_c/2mc^2)]^{\frac{1}{2}}} \quad (2.1)$$

where h is Planck's constant, m is the mass of the electron with charge e and c is the velocity of light. For the studies reported here, an accelerating voltage of 200 kV was used in the microscope, which corresponds to a relativistically corrected wavelength of 0.0251 Å.

In transmission electron microscopy a monochromatic electron beam is accelerated through a thin sample and several diffracted beams (along with the transmitted beam) are present at the exit surface of the specimen. These beams are then focused as described in Sec. 2.1.1. The purpose of this section is to develop the required framework for the interpretation on diffracted patterns, using simple geometrical concepts.

When the electron beam penetrates the sample, each individual atom contributes to the scattering of the incident beam. However, only for certain crystallographic directions is the scattering of the wavelets in phase (i.e. to contribute with one another, as in constructive interference). For this reason diffraction from a crystal must be discussed with regards to the phase relationships between the scattered waves of each atom.

We can borrow some principles commonly used to describe the diffraction of a monochromatic light source by a grating, to describe electron diffraction in a crystal. Without considering a full three-dimensional crystal, we will use the analogy of a one dimensional grating as shown in Fig. 2.3. In this drawing, a grating consisting of a series of slits and alternating plates (infinite in the direction into and out of the paper) of spacing a . An image screen (denoted as AB) is placed at a large distance (R) from the grating. Any waves which scattering in phase from the opening OP will result in a bright spot at point X . For the waves to scatter in phase, their pathlength difference, OD must be an integer multiple of their wavelength λ . For all other points on the screen, where the pathlength difference varies, the intensity on the screen will vary according to this difference. If the waves are completely out of phase, then no intensity will be observed, while various phases will result in lower intensities than for

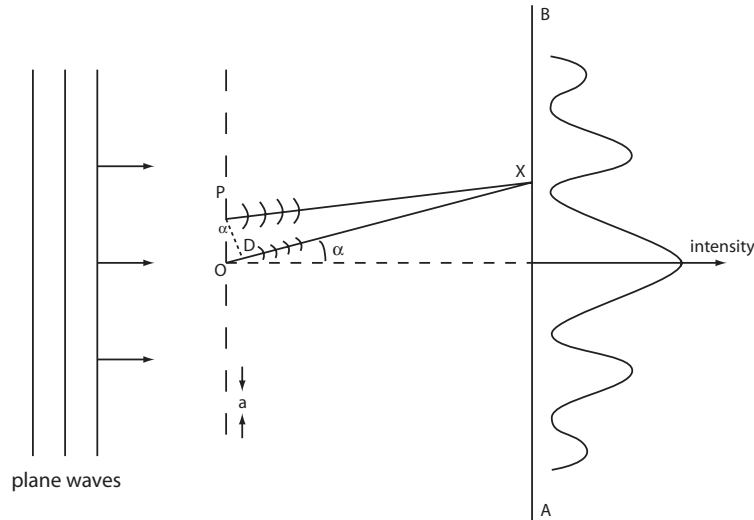


Figure 2.3: Schematic diagrams of monochromatic diffraction of light by a line grating with slit width a .

the case of completely in phase waves. When observing the interference effect over the entire screen, alternating bright and dark lines appear perpendicular to the plane of the paper. The approximate intensity distribution that results is also shown in Fig. 2.3. As the angle α increases the fringe intensity decreases as a consequence of reduced scattering efficiency through large angles. For a three-dimensional crystal, by analogy, a pathlength difference argument may be used to describe the diffraction of the electron beam to form an interference pattern composed of beams, rather than lines.

Most of the results of electron diffraction experiments can be explained using kinematical theory, which makes the following assumptions [22]:

- A monochromatic electron source.
- A Distortion free crystal.
- Scattering of the incident beam by the crystal is negligible, i.e. each atom experiences an incident wave of the same amplitude.
- Incident and scattered waves are plane waves.
- There is no absorption of the electron beam as it passes through the crystal.

- The incident and scattered waves do not interact with each other.
- There are no multiple scattering events.

Although these assumptions are never completely true in the microscope, the kinematical treatment of electron diffraction is satisfactory for the purposes of understanding the results of this study.

2.1.2.1 Bragg's Law

It has been mentioned that diffracted beams are a result of the interference of waves that are in phase within the crystal. This interpretation can be visualized schematically in Fig. 2.4a. What follows from this treatment is Bragg's law for diffraction. It is important to note that electron diffraction can only be treated in the limit of Bragg's law, for cases where the crystal is typically 1000–3000 Å thick. For the situation depicted (Fig. 2.4a) a particular sample is setup in transmission geometry, with an incident beam of electrons (treated as plane waves) with an angle of incidence Θ , relative to the two (hkl) crystal planes, I and II. The two incident waves are then reflected by these crystal planes at an angle Θ . At the exit plane wave front CD , two situations may arise.

1. If the two waves are in phase, as in Fig. 2.4a, then constructive interference will result in a strong reflected beam.
2. If the two waves are out of phase, then they will interfere with each other, and will result in either no beam or a very weakly reflected beam.

For the strong reflection situation (1), the pathlength difference POD must be an integer multiple (n) of the wavelength λ , i.e. $n\lambda$. From simple geometry, it is easy to show that $PD = OD = OL \sin \Theta$, and simplifying: $2OL \sin \Theta = n\lambda$ for strong reflections. In crystallographic terms, OL is the interplanar spacing d_{hkl} . Therefore, for the strong beam condition we require

$$2d_{(hkl)} \sin \Theta = n\lambda. \quad (2.2)$$

Eq. 2.2 is known as Bragg's law. The consequence of this derivation is that, strong diffracted beams will only result on the exit side of the crystal if there is a set of crystal planes oriented at the appropriate angle Θ relative to the incident beam. In our kinematical treatment, we can assume that the crystal poorly reflects the transmitted beam, and that some electrons do not undergo these processes, but are simply transmitted through the sample. As a result,

2.1 Transmission Electron Microscopy

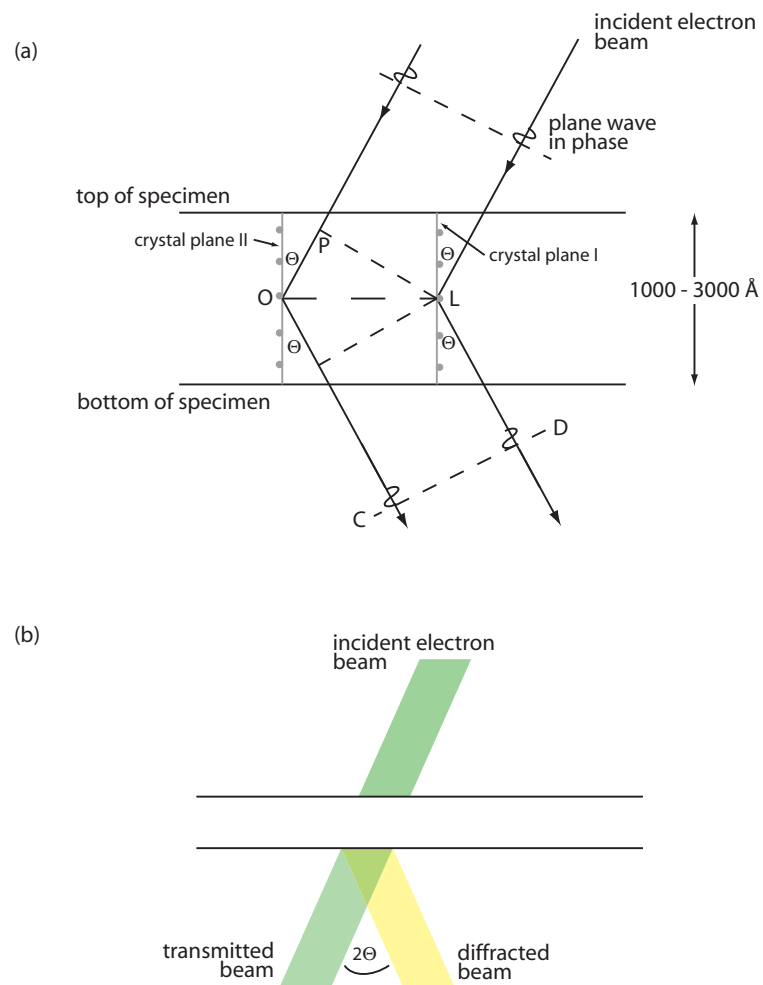


Figure 2.4: (a) Schematic illustration of Bragg reflection in a crystal at an angle Θ from two crystal planes, and (b) the relationship of the incident, transmitted and diffracted beams in transmission geometry.

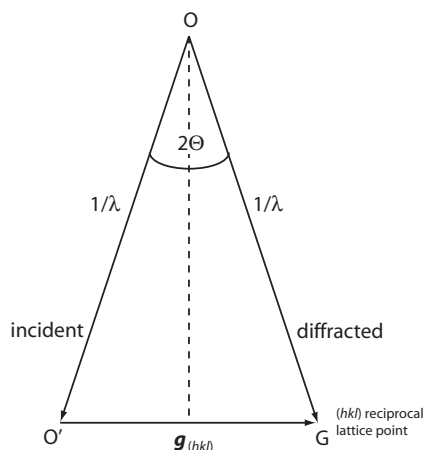


Figure 2.5: Reciprocal space vector diagram describing the reflection by a set of (hkl) planes.

at the exit surface of the specimen a transmitted beam and reflected beam will be found, separated by an angle 2Θ (Fig. 2.4b). In Bragg's law treatment of electron diffraction, diffracted beams are referred to as reflected beams.

2.1.2.2 The Ewald Sphere Construction

To understand the intensities associated with diffraction patterns we can take Bragg's law and incorporate the Ewald sphere construction along with the reciprocal space lattice. To help describe single crystal diffraction, the use of the reciprocal lattice is helpful. Essentially, it consists of points, corresponding to particular (hkl) planes, that are a distance $|\mathbf{g}| = 1/d_{(hkl)}$ from the origin in a direction perpendicular to the (hkl) planes. The reciprocal lattice effectively provides a map of the diffracted intensity distribution in reciprocal space.

For a unit incident wave vector ($\mathbf{k} = 1$) the diffracted beam can be found by constructing a vector triangle, as shown in Fig. 2.5. A line corresponding to the incident beam with magnitude $1/\lambda$ starts from a point, O in the reciprocal lattice and ends at the origin of the reciprocal lattice O' . A line OG of magnitude $1/\lambda$ can be drawn from O to the reciprocal lattice point G which is described by the vector $\mathbf{g}_{(hkl)}$ for the crystal plane (hkl) . Since the reciprocal lattice is three-dimensional and OO' and OG are of equal length, the illustration in Fig. 2.5, represents only a fraction of a sphere with radius $1/\lambda$ in reciprocal space. This construct is known as the Ewald or reflecting sphere. This interpretation is important since it allows one to describe the form of the diffraction pattern for a given incident beam direction in the crystal.

2.1 Transmission Electron Microscopy

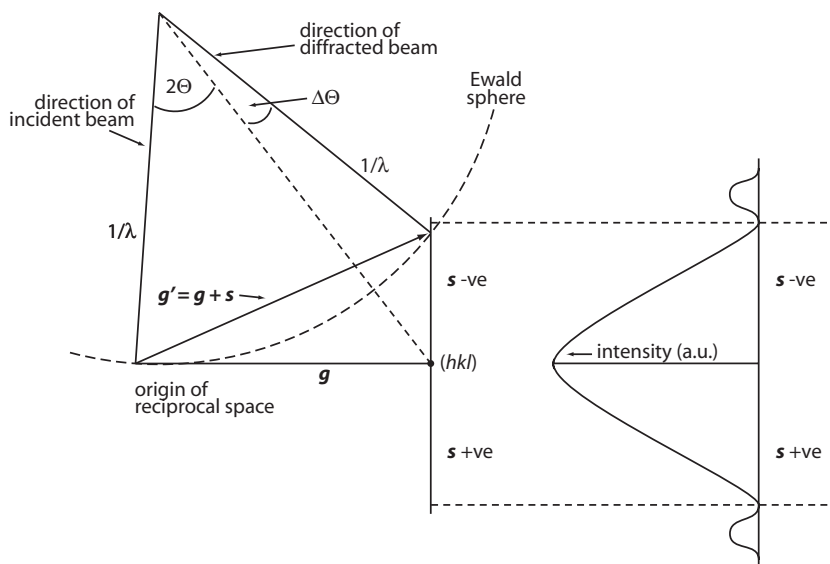


Figure 2.6: Ewald sphere construction for a reciprocal lattice point (hkl) showing how the intensity of a diffracted beam deviates from the ideal Bragg condition.

In order to properly describe the diffraction pattern with the Ewald construction, a slight modification of the reciprocal lattice is required owing to the geometry of the sample, i.e. a thin sheet of material. It can be shown, but will not be derived here, that the width of a reciprocal lattice point scales as $2/N_i$, where N is the number of unit cells along the i direction [23]. Since a TEM sample may be considered as a semi-infinite material, that is, effectively infinite in the xy -plane, but finite (≈ 500 unit cells) along the z -direction (the direction of the electron beam), the reciprocal lattice points are anisotropic in each direction. Consequently, the reciprocal lattice points are very narrow in the x - and y -directions, while in the z -direction they are much broader. For this reason, the reciprocal lattice points must be considered as streaks in the z -direction. This fact relaxes the Bragg condition required for diffraction, and even if the Bragg condition is not met exactly, diffracted intensity will be observed. The corrected Ewald sphere construction, which considers the anisotropy in the widths of the reciprocal lattice points is shown in Fig. 2.6. The deviation from the exact Bragg condition is given by the vector \mathbf{s} which describes the deviation from the Bragg condition as the Ewald sphere cuts through the reciprocal lattice point. As \mathbf{s} increases the diffracted intensity decreases as illustrated

2.1 Transmission Electron Microscopy

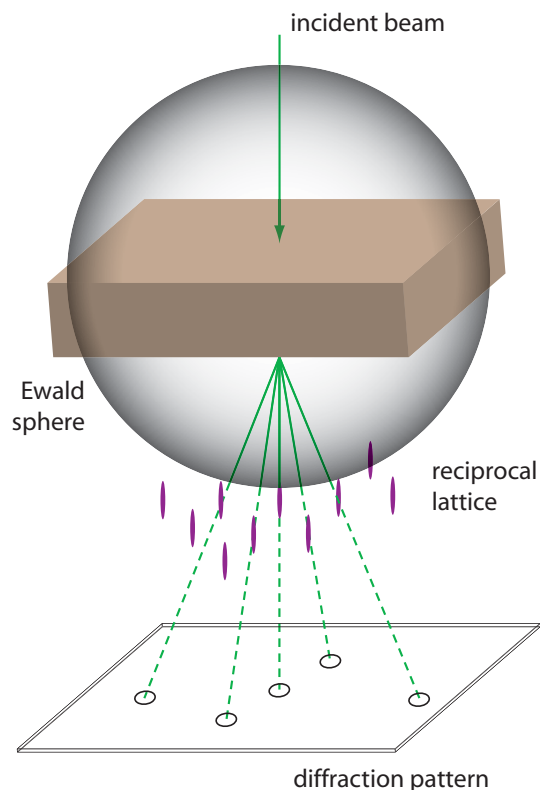


Figure 2.7: The Ewald sphere construction in reciprocal space shown schematically with the specimen, transmitted and diffracted beams, along with the resultant diffraction pattern.

in Fig. 2.6, for the case where $\mathbf{s} \neq 0$ the reciprocal lattice vector is given by $\mathbf{g}' = \mathbf{g} + \mathbf{s}$.

The purpose of discussing the Ewald sphere and the reciprocal lattice is shown in Fig. 2.7. Despite this being a cartoon which helps with understanding the formation of a diffraction pattern, it serves a greater purpose. In Fig. 2.7, the Ewald sphere is schematically shown to be centered about the specimen where the diffraction occurs, along with streaked reciprocal lattice points (to compensate for the specimen thickness). For an incident 200 kV electron probe, $1/\lambda = 39.87 \text{ \AA}^{-1}$, but typical reciprocal lattice spacings $1/d$ are about 0.5 \AA^{-1} . One can deduce that the Ewald sphere is nearly 80X greater than the spacing between reciprocal lattice points. As a result, the Ewald sphere is nearly flat as it intersects the reciprocal lattice. This consequence enables several reciprocal lattice points to be cut simultaneously and results in several diffracted beams which produce the diffraction pattern.

2.1.2.3 Selected Area Diffraction

Most often times information from a specific region of a sample is desired. The diffraction technique which enables the extraction of this type of data is known as selected area diffraction (SAD). The geometry of this process is shown in Fig. 2.2a. As previously described, a specimen is illuminated with an electron probe which results in both transmitted and diffracted beams, which contribute to the diffraction pattern observed in the back focal plane of the objective lens. However an aperture can be inserted coplanar with the image, limiting the the number of beams which contribute to the diffraction pattern. This aperture allows only those beams which are selected to produce the diffraction pattern on the phosphor screen, while all electron beams passing through the sample still contribute to the diffraction pattern formed at the back focal plane.

It is important to note that the use of a selected aperture may introduce errors into the diffraction pattern due to contribution of beams outside the area of the aperture. This can occur if the aperture is not coplanar with the image and positioned as in Fig. 2.2a, denoted by X-X, relative to the image. Additionally, spherical aberrations may also result in a non-coplanar selected aperture: as a consequence of the focal length of the objective lens changing as it crosses the aperture. Another effect of the objective lens that is worth mentioning is that it rotates the image 180° relative the diffraction pattern. For instance, a vector \mathbf{g} can be defined which corresponds to a reciprocal lattice vector, and by definition is normal to the plane which it defines, i.e. the real space crystal lattice plane. Consistent with this interpretation, one can describe the same \mathbf{g} to point for the transmitted to diffracted beam. The directions of \mathbf{g} at the object and image are shown in Fig. 2.2a. As is shown, the objective lens rotates \mathbf{g} by 180° in the image relative to the object, but this rotation does not occur for the diffraction pattern. When interpreting images and diffraction patterns together, one must be cognizant of this effect (some microscopes correct for this rotation).

2.1.3 Image Formation

Before discussing the two common imaging modes, it is important to summarize a few fundamentals of image contrast theory and image formation. Essentially image formation is a result of the electrons that are transmitted through the sample, while contrast in the image is an artifact of the scattering (and absorption) of the incident electrons by the specimen. It is important to make

2.1 Transmission Electron Microscopy

the distinction between the contrast we are use to seeing (as in an optical light microscope) and that of a TEM image. In the electron microscope, the material interacts with the electron probe mostly through diffraction, as opposed to absorption; albeit, the intensity of the transmitted beam is still affected by the density (and volume) of the sample which is passes through.

Plainly, a thicker (denser) sample will inelastically scatter more electrons than thinner regions. As a consequence less electrons will exit the specimen surface from these thicker regions, and contribute less to the formation of the image. Therefore thicker samples will appear darker in the image on the phosphor screen. One word of caution is that this is a generalization, and by no means absolute. Sample orientation can mislead one into thinking that a thin material is actually thick as has been reported for some nanoparticles known as rafts.

Image contrast in the microscope can be attributed to two effects: (1) Diffraction contrast and (2) Phase contrast. I will briefly summarize the mechanism herein, but refer the reader to the literature for a more thorough analysis of contrast theories [20–22].

2.1.3.1 *Diffraction Contrast*

As diffracted electrons exit the specimen, they may be collected by the objective aperture and prevented from contributing to the image. By selecting whether or not to include various diffracted beams from the sample, a bright field (BF) or dark field (DF) image may be formed (cf. Sec. 2.1.3.3). Diffraction contrast is one of the dominate materials characterization techniques for studying defects in crystals, and is the principle contributor for contrast in crystalline specimens.

Essentially, bright field images exclude diffracted electrons, while dark field images exclude transmitted electrons. The image that is produced is a projected map of the intensity distribution across the transmitted and diffracted beams (just highly magnified) which results between the interaction of the incident electron probe and the sample. Consequently, the image contrast in this case is attributed to the differences in the efficiency at which the specimen diffracts electrons. For this reason, image interpretation is closely linked with diffraction theory.

2.1 Transmission Electron Microscopy

2.1.3.2 *Phase Contrast*

This effect is a result of different electrons recombining to form the image as they leave the surface of the specimen. Here, the phase differences at the sample are transformed into intensity differences in the image. This mechanism is responsible for much of the contrast observed at length scales less than 15 Å. For this effect to be important, most of the electrons which are scattered by the specimen must recombine with transmitted electrons after passing through the objective lens, in order to produce any intensity differences. For instance, this could be the recombination of one diffracted beam with the transmitted beam.

The effect of phase contrast in the image will, in part, be determined by how much the specimen introduces phase changes in the scattered electrons. The phase shift can be shown to be the result of the interaction of an electron wave with the projected potential of the specimen. For this reason, phase contrast images are sensitive not to atomic displacements, but rather variations in the electronic potential of the material being investigated. For more information cf. Ref. [24].

2.1.3.3 *Bright and Dark Field Images*

As mentioned, BF and DF imaging modes are very useful for examining microstructure and crystalline defects. The differences between forming BF and DF images can be seen by the ray diagrams drawn in Fig. 2.2.

In order to form a bright field image, an aperture may be inserted in the back focal plane of the objective lens to prohibit the diffracted beams from forming the image, and allowing only the transmitted beam through. On the other hand, the objective aperture may be displaced from the optic axis to permit only the diffracted beam to contribute to the image, while the transmitted beam is intercepted. This is known as a displaced aperture DF image, and usually results in poorer resolution owing to the increased effect of spherical aberration and astigmatism as the electron beam deviates from the optic axis. Shown in Fig. 2.2c is a centered DF image, which enables resolution similar to a BF image to be achieved. In this case, the illumination source is tilted, so that diffracted electrons travel along the optic axis, alternatively to transmitted electrons.

2.2 Sample Preparation

Standard TEM sample preparation techniques were used to produce specimens throughout experimentation. Care was taken to maintain as clean a preparation environment as possible since contamination of foreign species (carbon, alkaline earths and transition metals) can act as adatoms on surfaces being investigated. Samples were treated as if they were going to be used in a UHV chamber, therefore all materials and tweezers were kept in a clean dust free environment, wrapped with lint-free cloths or aluminum foil. Breathing on samples was also minimized to reduce deposit of carbonaceous residue which may prevent imaging of a reconstructed surface. Single crystal LaAlO_3 (001) wafers with dimensions of $10 \times 10 \times 0.5 \text{ mm}^3$ and EPI polished on one side were purchased from MTI Corporation (99.95% pure).

The wafers were cut into 3mm disc (nominal TEM size) using a circular disc cutter. The discs were then mechanically polished using 600 grit SiC paper to a thickness of approximately $100 \mu\text{m}$. Subsequently, each disc was mechanically dimpled so that the center sample thickness was approximately $10 \mu\text{m}$. Water-based polishing slurries were used during the dimpling process with incrementally finer particle size dispersions ($1 \mu\text{m}$ water-based diamond and $0.05 \mu\text{m}$ alumina suspension). Each sample was then thinned to electron transparency using a Gatan Precision Ion Polishing System (PIPS) with 4.8 kV Ar^+ ions at angles of incidence in the range of $80\text{--}85^\circ$ from the surface normal.

After ion milling, the surfaces and near-surface region are non-stoichiometric, oxygen deficient, severely disordered or under stress and contain bulk defects. The degree of surface damage due to sample preparation is material specific and the effects of ion milling on surface reconstructions is a topic under investigation in our group. In order to remove the damage inflicted from ion bombardment and achieve a stoichiometric flat surface for analysis, the oxide samples were annealed at atmospheric pressure at 30–70% of the melting temperature of the material, in order to limit bulk, but encourage surface diffusion. If bulk diffusion dominates, coarsening of the sample results and consequently useful TEM diffraction data is difficult to obtain. It should be mentioned, that the partial pressure of oxygen was not measured precisely, but it is taken to be close to the partial pressure of oxygen in air. The effects of the partial pressure of oxygen on surface reconstructions is also the topic of a current study [25].

Annealing treatments were carried out in a Carbolite STF 15/51/180 tube furnace with a maximum operating temperature of 1515°C . Samples were placed

2.3 Obtaining Surface Specific Information

inside of an alumina combustion boat which was placed inside of a clean quartz tube. The entire assembly is then placed in the alumina furnace. For this study, each end of the tube was left open to ambient air. The alumina boat and quartz tube were regularly cleaned with *aqua regia* (HCl + HNO₃), washed with deionized water, and dried using acetone and methanol. Following cleaning, the boat and tube were treated at 300°C for one hour prior to use to remove any carbonaceous residues. Dwell times at the maximum temperature depended on the sample under study, its thickness and degree of ion damage. All specimens examined used identical ramp-up and -down rates of 5° per minute and 8° per minute, respectively, to avoid thermal shock to the samples and furnace. The temperature range explored for LaAlO₃ was between 900–1500°C. Soak times ranged from 3 to 6 hours, however 3 hours was deemed sufficient time to achieve a ordered and reproducible surface structure.

2.3 Obtaining Surface Specific Information

Transmission electron microscopy has historically been used only as an instrument to obtain bulk information about a material, but as of late has been found extremely successfully at obtaining surface information. One of the first reported TEM surface studies was done in UHV by Yagi, *et al.* on the formation of Pd nucleus on Ag(111) surfaces [26]. Complete reviews of the study of surfaces through electron microscopy and diffraction techniques has been compiled in the literature and demonstrates the feasibility of investigating the atomic scale structure of materials at interfaces [27–30].

Of particular importance in this study is transmission electron diffraction (TED) which is quite successful at determining surface unit cell dimensions. As a result of dynamical scattering from the bulk when a sample is aligned along a crystallographic zone axis, relatively weak surface spots result, and consequently the sample must be tilted far off-zone to a more kinematical diffraction condition. Surface contrast is also enhanced as the specimen is tilted off-zone [31]. Examination of a thin sample using selected-area diffraction (SAD) or focused probe diffraction (FPD) at an off-zone condition easily reveals the surface spots. As the sample is tilted off-zone, an increase in the surface signal intensity relative to the bulk is observed due to truncation of bulk rel-rods in reciprocal space [23]. The additional reduction of dynamical effects improves the ability to recovery phase information for direct methods

2.3 Obtaining Surface Specific Information

(DM). Once the surface unit cell dimensions are found, determination of surface atom positions is pursued with a combination of DM, dark-field imaging and other spectroscopic techniques.

The surface imaging modes used in the study are categorized as plan-view imaging. In this experimental setup, samples are viewed parallel to the surface normal direction, where the transmitted beam interacts with the entire sample. Surface information can be extracted in a relatively straightforward manner, and all imaging modes available to the TEM can be implemented, including bright-field (BF), dark-field (DF) and HREM.

In this research, two diffraction techniques were used to probe the surface of LaAlO_3 . When the beam strikes the sample, the diffraction pattern contains information from the whole specimen. Often times the specimen is buckled and the resulting diffraction pattern is not very useful. To reduce the area of the beam interacting with the specimen as well as the intensity of the diffraction pattern, the beam can either be reduced with an aperture or condensed. The former technique is referred to as selected-area diffraction (SAD) and maintains the beam's parallelism. In this mode, a small aperture is used in the first image plane below the objective lens, but patterns that result may provide false intensities and complicate structure solution analysis [23]. As mentioned previously, the difficulty arises due to microscope imperfections such as spherical aberration of the objective lens or from regions outside the aperture contributing to the image. For this reason, the focused probe technique is used when capturing a series of negatives for analysis with DM. The focused probe diffraction (FPD) or microdiffraction requires forming a smaller diffraction probe above the sample with a small condenser aperture and small probe size. However, converging the beam destroys its parallelism and spots in the pattern are spread into discs.

2.3.1 Diffraction Analysis

After annealing, the samples were examined with TEM to characterize the surface. These methods were discussed above. Both BF and DF images were used to characterize the surface, while diffraction patterns were used to obtain information about the atomic structure of the surface. While high resolution real space imaging provides atomic scale information, it is insufficient at providing the necessary surface information for determining surface structures. A more robust means of resolving surface structural information involves the

2.4 The Crystallographic Phase Problem

use of a set of techniques known as direct methods (DM). This is the topic of the Sec. 2.4

High resolution electron microscopy images¹ were obtained with the Jeol 2100F Schottky FEG-TEM operating at 200 kV. Off-zone axis electron diffraction patterns and BF/DF images were obtained using the Hitachi 8100 electron microscope operating at 200 kV at Northwestern University. Negatives with exposure times ranging from 0.5 to 90 seconds were recorded for the the LAO (001) surface, since typically the intensities of diffraction spots vary over several orders of magnitude. Each negative was digitized to 8-bits with a 25 μm pixel size on an Optronics P-1000 microdensitometer and calibrated to be linear over the selected exposure range. Relative intensity measurements using a cross-correlation technique developed in our group and image processing was preformed using ELECTRON DIRECT METHODS (EDM 2.0) [12, 32]. The multiple reflection data sets were then symmetry reduced to provide a single set of independent beams. A corresponding error for each reflection was assigned using standard statistical methods [13]. Final structure investigations used the PEAKS code to determine surface unit cell contents [32].

2.4 The Crystallographic Phase Problem

The diffraction pattern that is observed in a scattering experiment is a product of the electron density of a crystal (for x-ray diffraction) or the crystal potential (for transmission electron diffraction). However, in a scattering experiment only moduli are measured and not the phases of the diffracted beams—this is the crystallographic *phase problem*. Since the phases of diffracted beams are lost in a TEM experiment, and only intensities are measured, phase relationships must be recovered to solve the structure directly. By taking the square root of the diffracted intensities, the moduli of the structure factors can be found. If both phase and amplitude of the diffracted beams were known, the structure factor would be completely described and Fourier analysis would produce correct scattering potential maps.

To illustrate this point, a structure may be project into a two-dimensions and represented by a function $f(\mathbf{r})$, where $\mathbf{r} = x\mathbf{a} + y\mathbf{b}$, and \mathbf{a} and \mathbf{b} represent

¹This work was done in collaboration with [Dr. Yingmin Wang](#)

2.4 The Crystallographic Phase Problem

real space lattice vectors. In a diffraction experiment, information about the object function is described by Fourier transforms, namely

$$f(\mathbf{r}) = \int_{-\infty}^{\infty} F(\mathbf{k})e^{2\pi i\mathbf{k}\cdot\mathbf{r}}d\mathbf{k} \quad (2.3)$$

$$F(\mathbf{k}) = \int_{-\infty}^{\infty} F(\mathbf{r})e^{-2\pi i\mathbf{k}\cdot\mathbf{r}}d\mathbf{r}, \quad (2.4)$$

where $\mathbf{k} = h\mathbf{a}^* + k\mathbf{b}^*$ and \mathbf{a}^* and \mathbf{b}^* are reciprocal space lattice vectors. Since this has been defined as a crystal structure projection, the function $f(\mathbf{r})$ is a potential, since as mentioned in an electron diffraction experiment, the electron probe interacts with the electrostatic potential of the crystal. The Fourier transform of the real space crystal structure, $F(\mathbf{k})$ is composed of harmonic components (structure factors) which correspond to a reflection vector in reciprocal space \mathbf{g} . Each component (or structure factor) can be described in polar form as

$$|F(\mathbf{g})|e^{i\phi_{\mathbf{g}}}, \quad (2.5)$$

where $|F(\mathbf{g})|$ is the magnitude and $\phi_{\mathbf{g}}$ is the phase term of the structure factor. In the kinematical treatment of electron diffraction the intensities, $I(\mathbf{g})$, observed are related to the structure factor by $I(\mathbf{g}) = |F(\mathbf{g})|^2$, and it is clear that the phase terms are lost. Therefore, the crystallographic phase problem reduces to recovering these phases, and this concept is known as Direct Methods.

2.4.1 Electron Direct Methods

A complete explanation of electron Direct Methods (DM) techniques for surfaces is beyond the scope of this work, however an overview of the methodology is given. Broadly speaking, DM are a set of routines which enable the determination of an initial estimate of atomic positions in a crystal structure. These mathematical techniques have been around since the 1950s and have been extensively applied to solving bulk crystal structures using x-ray diffraction data [19, 33–36].

Rather than proposing various models which fit the diffraction data, DM provides a means to propose true structures. The former approach of suggesting models, is a closed set technique, in that refining to a true structure with high accuracy is constrained by the fact that it must be similar to the initial structure. The deviation in such models from refined structures is typically less than a few tenths of an angstrom [11], and the solution is not unique, in

2.4 The Crystallographic Phase Problem

the sense that it must be associated with an input structure. While knowing the chemistry at the surface of a material enables the proposition of such models, this approach is not as strongly grounded. Therefore, the largest challenge to the crystallographer is generating the set of potential structures (of which the true structure must belong) from which the refinement process can proceed.

Direct methods essentially is a global search mechanism that determines the set of feasible models for further refinement, thereby eliminating the guesswork. These routines provide a more intelligent approach to structure determination by exploiting statistical relationships between intensities and phases (of the stronger reflections) for the case of scattering from atom-like features. Plainly, direct methods uses *a priori* information to constrain the phases of the measured reflections; it is the phase component of the structure factor which enables the determination of atomic positions. For this reason, recovering the correct phases is more important than determining the absolute values of the moduli. While the problem seems rather daunting to recover the phases, since the number of permutations goes as 2^N , where N is the number of diffraction intensities (or phases) that must be recovered; it is a tractable problem. It is not shown here, but the phases cannot be completely random [11]. Additionally, because the intensities do not have to be very close to their correct values, the problem becomes more encouraging to solve. In fact, the intensities can vary quite substantially, as long as the recovered phases are similar to the true values, the structure can still be identified.

With many practical scattering problems, as in electromagnetism, optics and imaging, they naturally arise as *inverse problems*, where the positions of the scatters have to be determined only from a measured (or desired) output signal. What all these problems have in common is that they share four basic elements [37] for recovering a solution:

1. A data formation model
2. *A priori* information
3. A recovery criterion, and
4. A solution method

2.4 The Crystallographic Phase Problem

These criteria can be applied to the crystallographic problem since the relationship between the scatters and the atomic positions is known (Criterion 1); the number of atoms may be known (Criterion 2); probabilistic relationships and iterative solution techniques exist (Criteria 3 and 4).

Direct methods enable rapid convergence to a small set of plausible solutions using reliable intensity data by constraining the solution set appropriately for crystal structures. More formally, to quote A. Subramanian and L.D. Marks [7] the constraints are

1. Atomicity: The scattering originates from atoms and therefore the solution should have atomic features; i.e. regions with peak-like charge densities corresponding to isolated atom charge densities.
2. Cell Density: Most of the charge density in the unit cell is zero: peak intensities are separated by charge free regions.
3. Positivity: Charge density in a real crystal is always positive.
4. Localization: The region of space with significant atomic displacements from bulk positions is limited to the near-surface region.

The recovered phases can then be compared against how well they obey these constraints by using a *Figure of Merit* (FOM). This FOM measures the effectiveness of the phase recovery algorithm and ultimately determines when the algorithm has satisfactorily refined the phases. The constraints are then imposed iteratively using the Gerchberg-Saxton method [38] and the projection onto convex sets algorithm [39] to refine the phases of the measured reflections. A genetic search algorithm [13, 40] then spans the solution space to identify the best solutions from the DM analysis. These solutions can then be used to generate scattering potential maps (for electron diffraction data) or charge density maps (for x-ray diffraction data). Atoms are then assigned to regions of high intensities in the maps, and a set of working initial models (as discussed previously) can be refined until a stable structure is reached.

In some cases, the surface reflections overlap with bulk reflections or those which have contributions from other surface domains. When this occurs, only a portion of the structure may be identified due to the unmeasured (or missing) reflections and experimental errors. Nonetheless, structure completion, i.e. refinement, is accomplished through various techniques including Fourier-difference methods and projected-based methods [41] through the PEAKS code,

2.4 The Crystallographic Phase Problem

integrated into EDM 2.0. Feasible structures that have been determined through these methods are then further refined using a standard Crystallographic R-factor (residual) or χ^2 estimator against the experimental data according to

$$R = \frac{\sum I_M - \alpha I_C}{\sum I_M} \quad (2.6)$$

$$\chi^2 = \frac{1}{N - V} \sum \left(\frac{I_M - \alpha I_C}{\sigma} \right)^2 \quad (2.7)$$

where I_C and I_M are the calculated and measured intensities, respectively, N is the number of data points, V is the number of variable parameters in the refinement, and σ is the error associated with the experimentally measured data.

Final refinements and evaluation of the structure stability is performed with a combination of *ab initio* density functional calculations and multislice simulations for self-consistency.

CHAPTER 3

Reconstructions on the LaAlO_3 (001) Surface

3.1 Background

3.1.1 *The Perovskite Crystal Structure*

Lanthanum aluminate (LaAlO_3 , LAO) is selected for investigation due to its importance as a model catalytic oxide and since it acts as an optimal substrate for epitaxial growth of high temperature superconductors, ferroelectric thin films, and magnetic oxides [42, 43]. This mixed metal oxide is representative of a larger class of materials with ABO_3 stoichiometry known as perovskites, where the A-site cation is usually an alkali or alkaline earth, and the B-site cation is typically a transition metal. The perovskite structure comprises a simple cubic lattice of the A-site cation with a B-site cation in the body center (Fig. 3.1).

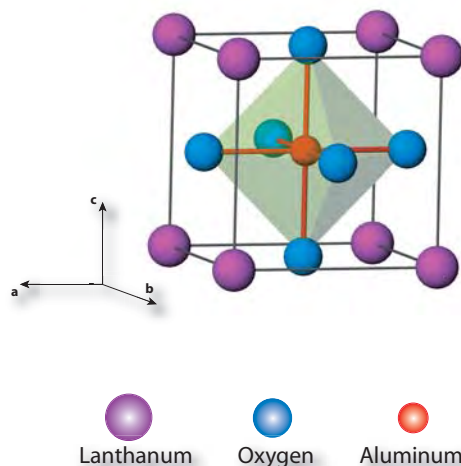


Figure 3.1: *The ideal ABX_3 cubic perovskite structure illustrating the octahedral coordination of the B-site (aluminum here) cations (for LaAlO_3).*

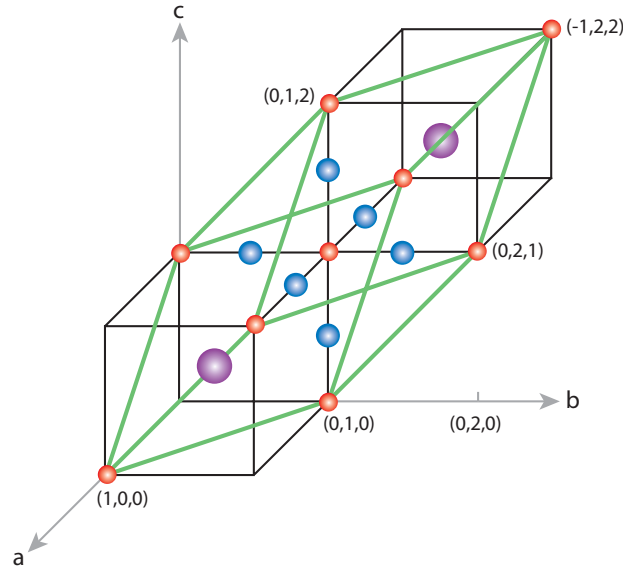


Figure 3.2: The low temperature LaAlO_3 rhombohedral unit cell (outlined in green) is shown relative to the cubic perovskite (outlined in black). NB.: bulk LAO contains two formula units at room temperature.

Oxygen anions are found at the face centers, thereby forming an octahedron with the B-site cation in the center of the unit cell. Bulk LAO has a rhombohedral perovskite structure belonging to the $D_{3d}^5 - R\bar{3}c$ space group with a unit cell containing two formula units at room temperature ($a = 5.357 \text{ \AA}$, $\alpha = 60^\circ 25'$) [44]. Distortions in the regular cubic geometry of the octahedral BO_6 and the dodecahedral AO_{12} result in the rhombohedral perovskite. The cubic to rhombohedral relationship is depicted in Fig. 3.2. It undergoes a transition at $435 \pm 25^\circ\text{C}$ to a simple cubic unit cell containing only one formula unit ($a = 3.821 \text{ \AA}$, $\alpha = 90^\circ$) [45]. The melting point for LAO is 2180°C and the rhombohedral to cubic phase transformation involves changes in bond angles of only tenths of a degree. At room temperature the BO_6 octahedra are tilted (rotated) about the crystal's triad axis. Essentially, as temperature increases the angle of rotation in the BO_6 octahedron continually decreases until it becomes zero [46]. This phase transition is completely second order in nature. For this reason, the rhombohedral unit cell is typically treated as pseudo-cubic ($a = 3.790 \text{ \AA}$, $\alpha = 90^\circ$). However, it is important to note that this crystal does

not have the full symmetry of a cubic material, owing to cation shifts. Consequently, throughout this work, we will maintain the rhombohedral notation of the crystal lattice. This seemingly subtle point has significant implications on the atomic and electronic structure of the material in regard to this work. This fact will be explored in more detail in further chapters.

3.1.2 Polar Surfaces

The composition, structure and morphology of LaAlO_3 (001) has been researched in the past few years; however, definitive structural information of how the surface terminates is still ambiguous [47–50]. The results by different research groups remain contradictory and few have proposed plausible surface structure models. In this brief review, the current state of research on this surface is discussed in the context of atomic structure.

At times, some surfaces of ionic or partly ionic crystals have the unique property that they are polar, i.e. there is a dipole moment in the unit cell normal to the surface. As classical electrostatics requires, such a dipole results in an infinite (diverging) surface energy [51]. One of the most straightforward ways of examining surfaces is by considering the crystal as stacks of planes. Using this method, the surface free energy (γ_i) can be calculated by taking the difference between the surface stack and the equivalent number of bulk ions composing the same area, or

$$\gamma_i = \frac{E_{\text{Surf}} - E_{\text{Bulk}}}{\text{Area}}. \quad (3.1)$$

As Tasker [52] illustrates, such polar surfaces can be classified into three types, with regard to the distribution of charge (q) and a dipole moment (μ) normal to the surface unit cell (Fig. 3.3). Type I surfaces have an overall charge of zero for each plane, since it is composed of both cations and anions in the correct stoichiometric ratio. A Type II surface is charged for each of its repeat units, but the net dipole is canceled by the adjacent planes, since each sublattice has an equal and opposite charge. In contrast, the Type III surface has a diverging electrostatic energy due to the presence of a dipole normal to the surface unit cell created by alternating charged planes. This dipole is present not only when the crystal is truncated between the adjacent planes, but is also present in the repeat unit cell which leads to an overall polarized electric field in the bulk [52].

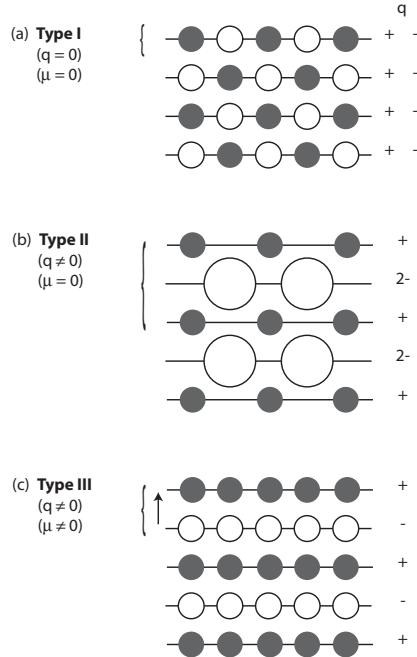


Figure 3.3: The three types of atomic configurations are shown, with the repeat unit bracketed: **(a)** Type I, equal number of cations and anions per atomic plane; **(b)** Type II, charged plane without a net dipole moment; **(c)** charged planes with a net dipole moment perpendicular to the surface.

LaAlO_3 (001) is of the Type III surface, and consists of alternating layers of LaO and AlO_2 stacked in the $\langle 001 \rangle$ cubic direction which is equivalent to the $\langle 11\bar{1} \rangle$ rhombohedral direction (Fig. 3.4). Consequently, the formal charges of La^{3+} , Al^{3+} and O^{2-} produce two terminations differing in nominal charges of $(\text{La-O})^+$ and $(\text{Al-O}_2)^-$. Clearly the layers are not charge neutral and an excess half electron (or hole) exists per unit interface cell. In the bulk material, the extra half charge is compensated by the adjacent layers above and below it. Therefore an AlO_2 terminated surface of LAO has a surplus half electron per (1×1) cubic unit cell. If this is treated in the rhombohedral unit cell, the surface terminates with an additional full electron (or hole). Since bulk truncation creates a dipole moment perpendicular to the unit cell, the surface must be stabilized to achieve a (near) charge neutral material.

Cancellation of the dipole moment can be accomplished through the following mechanisms:

1. Stoichiometry: If the surface's atoms remain in their bulk oxidation states, a change in the surface stoichiometry can balance the excess charge. Such

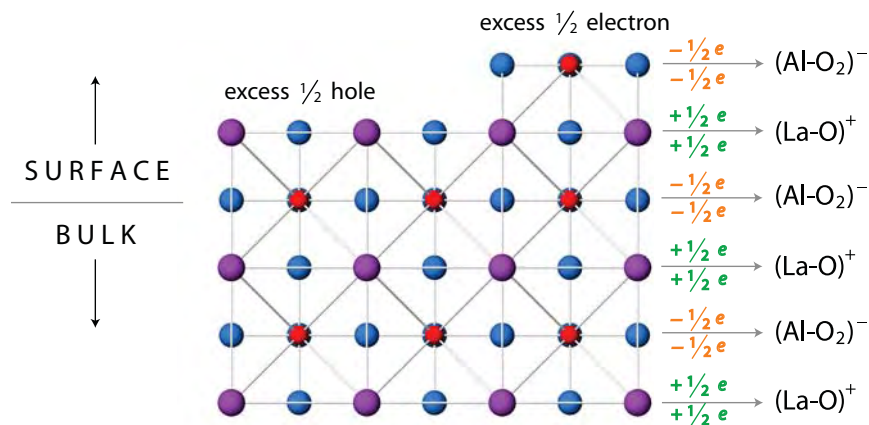


Figure 3.4: Alternating planes of LaO and AlO₂ are shown stacking in the < 001 > cubic direction. Simple electron counting models show that bulk termination leads to a polar surface requiring a charge compensating mechanism at the surface-vacuum interface.

stoichiometric changes are usually accompanied by a reconstruction consisting of a few atomic layers at the surface according to the arrangement of vacancies and adatoms.

2. Chemical: Adsorption of various chemical species from the environment, e.g. OH⁻ radicals can passivate the surface.
3. Electronic: The (near) surface electronic structure may be modified through a redistribution of electronic charge to cancel the polar electric field.

Polar oxide surfaces are an interesting class of Type III materials, because the cation-oxygen bonding may possess some covalent character. Furthermore, while these charge compensating mechanisms provide an initial place for understanding surface physics, there are no definitive methods for determining which mechanism works for different types of materials. Accordingly, the atomic structure of the surfaces are just as ambiguous. By using a material system like LaAlO₃ and a low-indexed crystal face, this study attempts to enlighten this complex problem.

3.1.3 Previous Surface Studies

Simple bulk termination of the LAO (001) surface suggests that it either terminates LaO_x⁻ or AlO_x⁻-type. Reflection electron microscopy (REM) studies by Wang and Shapiro have found that this surface terminates exclusively La-O or Al-O only [53]. This conclusion is based on the absence of difference

contrast in the REM images, since a mixed terminated surface would result in different scattering between the La and Al atoms. However, it was noted that precise termination of the surface was beyond the capability of the REM technique. As mentioned, such single termination cannot provide for the necessary charge compensation, and for this reason Wang and Shapiro suggested that the surface absorbs oxygen in order to satisfy electrostatic arguments, i.e. charge neutrality. In their model, only one oxygen atom is associated with either a La or Al atom. Consequently, they argue that the symmetry and valence of the cations is preserved (with respect to the bulk).

Several studies have been done in recent years by other groups which have shown that the surface termination is strongly influenced by the experimental conditions, e.g. temperature treatments. A summary of these results is included in Table 3.1 and the discussion of these experiments follows. For temperatures below 300°C, Yao *et al.* found that LAO (001) terminates Al-O₂ type from room temperature to approximately 150°C, and La-O type above 250°C [47, 57]. However, Jacobs *et al.* in their molecular dynamics simulations have reported that the La-O layer is more stable than the Al-O₂ layer at room temperature [54, 55]. For intermediate temperatures (150–250°C), mixed terminations are reported according to Yao *et al.* X-ray crystal rod truncation analysis performed by Francis *et al.* have found that at room temperature LAO is AlO₂ terminated with minor structural rearrangements consisting of oxygen relaxation away from the surface and aluminum atoms into the surface [48]. Conversely, near 400°C they have found structural rearrangement involving four atomic surface layers, while maintaining an Al-O₂ surface termination. Moreover, Schmidt and co-workers have found mixed terminations of La-O and Al-O₂ around 400°C through LEED, XPS and STM analysis [56]. In particular one base termination, either La-O or Al-O₂, was found with approximately half of the surface covered by single layer islands of the alternate termination.

Similarly, Kawanowa *et al.* reported mixed terminations at room temperature, and single LaO terminations at long anneal times near 700°C [49]. Step heights determined with atomic force microscopy confirm the results of their LEED experiments, and suggest that the terraces are approximately 1000 Å wide [47]. Time-of-flight scattering and recoiling spectrometry was used to determine the atomic species at the surface layer, and LEED was conducted on room temperature samples. From the diffraction data, sharp (1 × 1) patterns were

Surface Termination	Environment (torr)	Temperature (°C)	Analysis	Group
AlO _x	1×10^{-10a}	23	X-ray truncation rod analysis	Francis, <i>et al.</i> [48]
AlO _x	"	400		
AlO _x	1×10^{-10b}	23–150	AFM, LEED, XPS, TOF-SARS ^c	Yao, <i>et al.</i> [47]
AlO _x and LaO	"	150–250		
LaO	"	>250		
LaO (5 × 5) on AlO ₂	not reported	7	Molecular Dynamics Simulations	Jacobs <i>et al.</i> [54, 55]
AlO ₂ and LaO	2.25×10^{-10d}	23	LENS ^e	Kawanowa <i>et al.</i> [49]
LaO	2.25×10^{-7d}	727		
AlO ₂ and LaO	1×10^{-10f}	400	STM, XPS, ISS ^g	Schmidt <i>et al.</i> [56]
AlO ₂ or LaO (5 × 5)	$10^{-6} - 10^{-7h}$ $10^{-6} - 10^{-7i}$	1500 "	REM, RHEED	Wang and Shapiro [53]

^aSurface prepared by annealing in flowing O₂ at 1200°C and cleaning at ≈600°C for several hours

^bCleaned in UHV for several hours at 800°C

^cTime-of-flight scattering and recoiling spectrometry

^dSurface prepared by cleaning at 1000°C for 8 hours and annealing for 15 hours in UHV

^eLow energy neutral scattering spectroscopy

^fSurface annealed at 670°C with P_{O₂} = 5×10^{-5} torr for 25 minutes

^gIon scattering spectroscopy

^hSurface annealed for 10–20 hours

ⁱSurface annealed for 20 hours

Table 3.1: Summary of observed surface terminations (or reconstructions) on the LaAlO₃ (001) surface.

found for the low temperature experiments. This implies that the surface retained an ordered bulk structure. Yao *et al.* have proposed that the surface stoichiometry transition is a result of oxygen deficiencies upon heating. This effect creates a surface vacancy in the twelve coordinate site of the perovskite structure. For such oxygen deficient structures it has been proposed by Kawanowa *et al.* that the valence of La would be reduced from La^{3+} to La^{2+} [49]. Such valence change would produce a driving force for stabilization of the LaO layer rather than the AlO_2 layer.

With the presence of an electrically unstable dipole at the surface of LAO for single unreconstructed bulk terminations of LaO and AlO_2 , simple electron counting models [58] fail to construct any favorable terminations without supplemental passivating mechanisms. One such model which compensates for this surplus charge would be a mixed terminated surface layer that is half-occupied. However, the mixed termination must be less than the surface electrostatic screening length in order to fully cancel the dipole [56]. Half-occupancy on the order of less than 100 Å would be required; therefore, the 1000 Å wide terraces as suggested by Yao *et al.* would not be small enough to cancel the dipole. Alternative solutions for surface charge balance requires reconstruction and standard arguments include either a quarter monolayer of oxygen vacancies (for Al-O₂) or adatoms (for La-O). Similarly, a redistribution of the electron charge density in the near surface region of the crystal may reduce the dipole moment through a nominal charge transfer between the cations and anions, i.e. increased covalency at the surface.

Reported reconstructions on the (001) surface of LAO is limited, however RHEED and REM experiments by Wang and Shapiro have shown that a (5 × 5) reconstruction is obtained by annealing a surface sample at 1500°C for 20 hours in air [53, 59, 60]. Jacobs *et al.* investigated this reconstruction and concluded that the Al-O₂ surface layer reconstructs in a DAS structure, that is, it contains dimmers, adatoms and stacking faults [55]. In their unit cell, the adatoms are the outer Al atoms and only two layers participate in the reconstruction. AlO_2 clusters are bounded by La cations which are located at the bottom of pores formed in the unit cell. The La atoms appear to bridge two different domains of the reconstruction and have reduced coordination. Additionally, all Al atoms become tetrahedrally coordinated as opposed to their original octahedral coordination state by bonding to O anions in the layers closer to the bulk.

From these collected observations, it is clear that a comprehensive study of the $\text{LaAlO}_3(001)$ surface is required in order to understand how the surface terminates and which mechanisms allow for charge compensation. To date, all models have failed to offer any plausible stabilization pathways that are consistent with the experimental results. Since the experimental studies also suggest various surface terminations, this apparently simple perovskite material might be much more interesting than previously thought. For this reason, determining the atomic structure at the surface will enable a better understanding of fundamental surface dynamic concepts, i.e. what is the underlying driving force for reconstruction.

This chapter is the beginning of a more complete study on this surface and will focus on the $\text{LaAlO}_3(001)$ surface annealed in air. Through a combination of electron diffraction and BF/DF imaging the surface morphology and crystallographic structure is investigated. The remainder of this chapter is organized according to the different surface morphologies observed as the annealing temperature is increased. Following that discussion is a section on the structural investigation of the reconstructed surface.

3.2 TEM Surface Studies

3.2.1 *Disordered Surface*

Transmission electron microscopy samples were prepared as outlined in Sec. 2.2. Prior to annealing treatments and following ion milling the $\text{LaAlO}_3(001)$ near-surface regions are under stress and disordered. These strain effects are visible in the dark field image of the $\text{LaAlO}_3(001)$ surface (Fig. 3.5). In this image, bend contours (extinction contrast) and several defects near the edge of the sample are visible. An on-zone (SAD) pattern is shown in Fig. 3.6 illustrating the bulk diffraction spots. This diffraction pattern has been indexed to the rhombohedral crystal structure, which corresponds to the $[11\bar{1}]$ zone axis. Similarly, an off-zone surface sensitive diffraction pattern is shown in Fig. 3.7. Along with the bulk diffraction spots, a diffuse ring is also seen which is attributed to a stressed surface caused by the ion-milling process. This rather thick ring suggests that the surface layer does not consist of an order (1×1) structure but rather may be disordered.

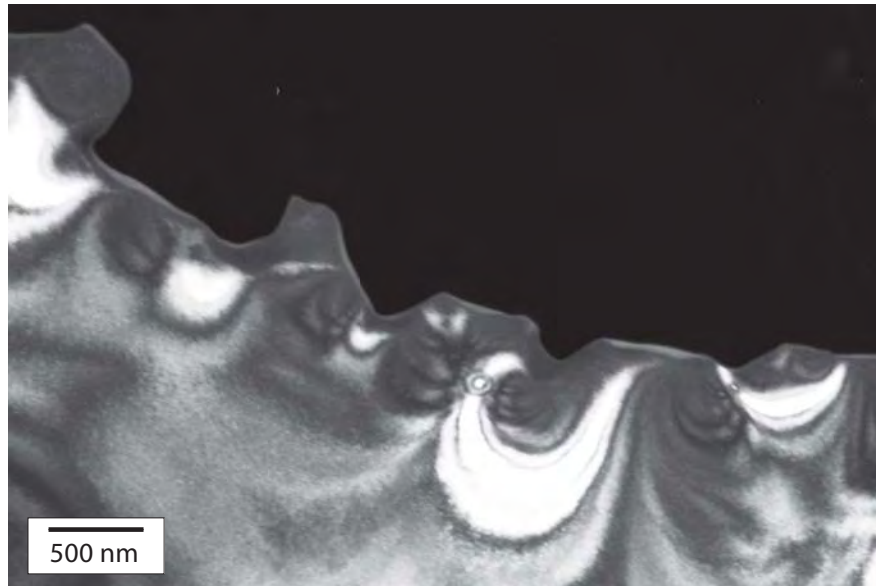


Figure 3.5: Dark-field TEM image of the $\text{LaAlO}_3(001)$ surface following the ion-milling process showing bend contours which suggests a stressed sample.

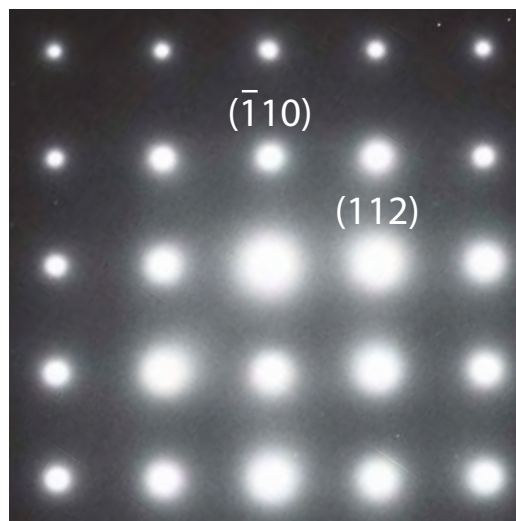


Figure 3.6: An on-zone $\text{LaAlO}_3(001)$ selected-area diffraction (SAD) pattern is shown prior to annealing treatments. NB.: the pattern is indexed to the rhombohedral unit cell, $[11\bar{1}]$ zone.

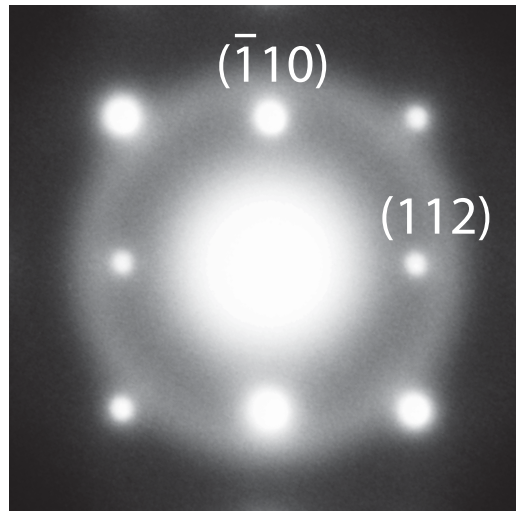


Figure 3.7: An off-zone SAD of the $\text{LaAlO}_3(001)$ surface prior to annealing and following Ar^+ ion bombardment. The diffuse ring around the bulk (1×1) spots is indicative of a disordered surface.

3.2.2 Recrystallized Surface

To reverse the damage caused by the ion-milling process and restore surface stoichiometry the crystals were annealed at approximately 1/3–1/2 of the bulk melting temperature. It was found that an annealing treatment for 3 hours at 800°C sufficiently recrystallized the surface, as illustrated by the absence of the diffuse ring in the off-zone diffraction pattern (Fig. 3.8). The (1×1) bulk unit cell has been outlined. At this temperature, it was found that there was sufficient energy to allow for surface diffusion and therefore the surface crystallinity was restored.

The surface morphology is characterized by preliminary faceting as shown in Fig. 3.9. The contrast in this dark field image is not attributed to stress but rather thickness variations in the sample, i.e. in the direction away from the hole. The surface also shows minor step bunches and the growth of terraces. The speckled contrast is attributed to voids in the near surface region and are further investigated in the Sec. 3.2.3.

3.2.3 Reconstructed Surface

Samples which were annealed at higher temperatures ranging from 1100°C to 1500°C (for 3 hours) exhibit a $(\sqrt{5} \times \sqrt{5})R26.6^\circ$ surface reconstruction. An example of a focused probe off-zone diffraction pattern of a sample treated at 1200°C is shown in Fig. 3.10. Not only are the bulk diffraction spots visible, but the presence of strong surface reflections are apparent. The (1×1) bulk

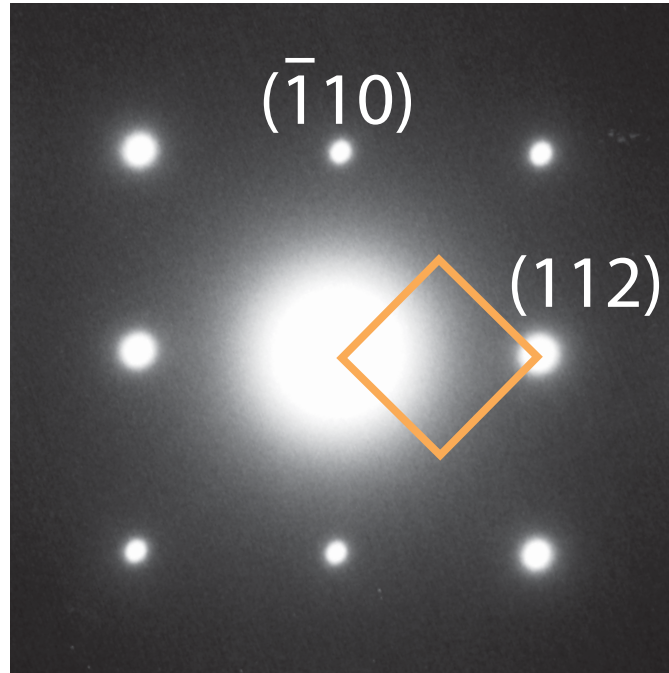


Figure 3.8: Annealing of the $\text{LaAlO}_3(001)$ surface at 800°C for 3 hours results in a recrystallized surface as illustrated by the absence of the diffuse ring in this off-zone SAD pattern. At this temperature no reconstruction is observed. The (1×1) bulk terminated rhombohedral surface unit cell is outlined.



Figure 3.9: Dark field image of the $\text{LAO}(001)$ surface after a 3 hour anneal at 800°C . Preliminary faceting is visible in the image. As the anneal time increases larger facets with fewer defects result.

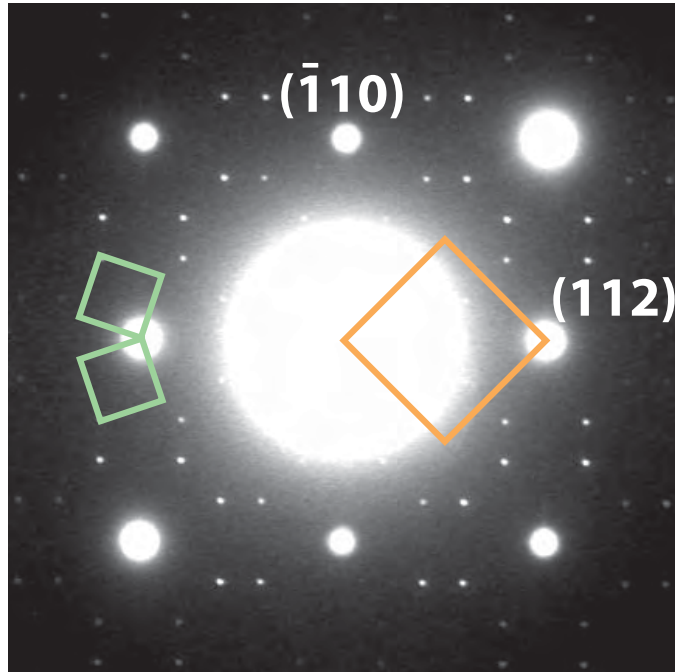


Figure 3.10: Annealing of LaAlO_3 (001) over the range of 1100°C to 1500°C for 3 hours results in a $(\sqrt{5} \times \sqrt{5})R26.6^\circ$ surface reconstruction with respect to the rhombohedral bulk unit cell. A focused probe off-zone diffraction pattern is shown with the rhombohedral (1×1) bulk unit cell (orange) and the surface unit cell for both domains of the reconstruction (green).

unit cell and the surface reconstruction unit cell have been outlined. It is interesting to note that there are two domains of this surface reconstruction, and after analysis it is clear that one domain is stronger than the other. This suggests that the superstructure spots may not be indexed to a larger unit cell. The unit cells for the reconstruction, which have been outlined, correspond to a centered unit cell (non-primitive) with respect to the rhombohedral bulk and are rotated 26.6° from the (1×1) bulk unit cell. In real space, this results in the largest possible surface unit cell, which tends to simplify the interpretation of the surface reconstruction. The domains relative to one another are rotated by 36.8° . This reconstruction has also been shown to be extremely reproducible (14 in the present study) and air stable for more than 6 months.

Fig. 3.11 is a dark field image obtained by annealing at 1100°C for 3 hours. The surface morphology shown is characteristic of that for all anneals over the range where the $(\sqrt{5} \times \sqrt{5})R26.6^\circ$ surface was observed, i.e. 1100°C to 1500°C . The surface exhibits extended faceting (cf. Fig. 3.12) with step bunches and reconstructed terraces. Based on the zone axis orientation, large $\langle 100 \rangle$



Figure 3.11: Dark field image of the $(\sqrt{5} \times \sqrt{5})R26.6^\circ$ surface on LAO after a 3 hour anneal (1100°C). The formation of $\langle 100 \rangle$ facets, with respect to the cubic face, occur at this temperature and can be seen in the image. Small rectangular features are discernible near the edge of the sample. These features do not show any strain contrast in the image which suggests they are not particles or trapped gas. Similar voids have been observed on other perovskite materials, like SrTiO_3 . This reconstruction is extremely reproducible and has been shown to be air stable for several months.

facets are observed on the surface. The dark and bright contrast variations are thickness fringes which result from rapid variation in the thickness of the sample toward the edge. Rectangular features are apparent at the edge of the sample and are suggested to be voids. These features are located in the near surface region and are characteristic of the manner in which the sample was prepared. These features do not show any strain contrast in the DF image which suggests that they are not particles or trapped gas. Similar voids have been shown to coexist on other perovskite materials that have been prepared in a similar fashion, like SrTiO_3 with its associated reconstructions [61].

It is important to recognize that the voids are not apart of the reconstruction and surface domains have been observed to cross the voids without perturbation. The voids themselves are not very deep, and this conclusion is based on the fact that as the sample thickness increases the void density remains the same. If they were thick, then the density should increase significantly for greater thicknesses. A high resolution electron microscopy image of the $(\sqrt{5} \times \sqrt{5})R26.6^\circ$ surface is shown in Fig. 3.12. The voids are typically on the

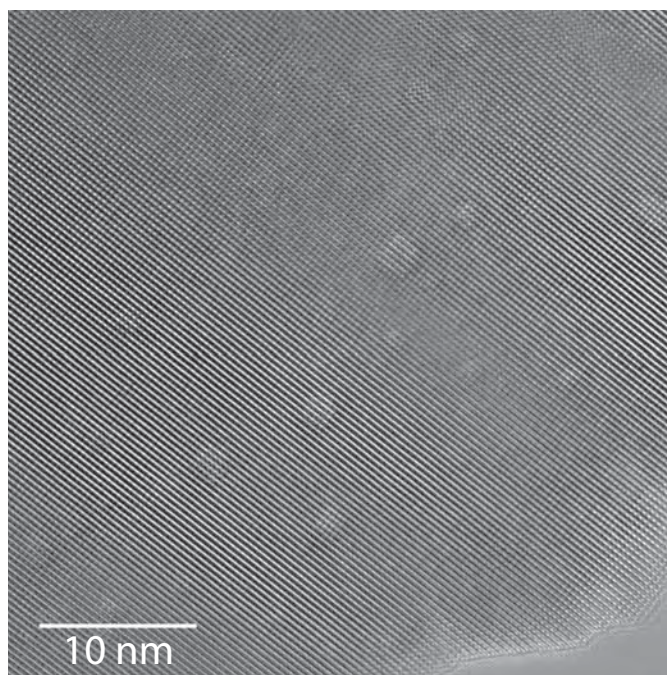


Figure 3.12: High resolution image of the LAO(001) surface after a 3 hour anneal at 1100°C. Faceting is visible along the edge and several voids are present throughout the sample.

order of $5 \times 5 \text{ nm}^2$ in size, and from previous multislice simulations are approximately 10 \AA below the surface layer [61].

3.3 Structure Completion and Refinement

This section discusses the atomic structure of the $(\sqrt{5} \times \sqrt{5})R26.6^\circ$ surface, current working models of the surface and refinement procedures.

As discussed in Sec. 2.3.1 diffraction data for the $(\sqrt{5} \times \sqrt{5})R26.6^\circ$ reconstruction was obtained by recording a series of negatives (in this case 7) at various exposures and then digitizing them. Then intensities of 7911 surface reflections were measured using the cross-correlation technique in EDM 2.0. The data set consisted of both strongly observed reflections and very weak reflections. This is a consequence of using a centered cell (non-primitive), where about half of the reflections should have little or almost no intensity.

These intensities were then averaged using $p2$ Patterson plane group symmetry to yield a set of 158 independent reflections (to 1.0 \AA resolution). Although $p2$ Patterson symmetry may also correspond to pm , pg , $p2mm$, $p2mg$ or $p2gg$ symmetries, they were ruled out due to the absence of mirror or glide planes in the surface diffraction pattern. Only the reflections within the range

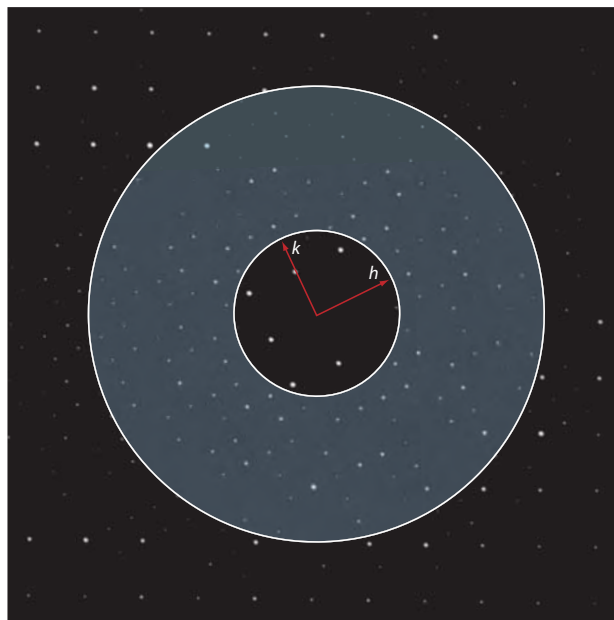


Figure 3.13: Surface diffraction pattern for the $(\sqrt{5} \times \sqrt{5})R26.6^\circ$ reconstruction. The annulus outlined in the diffraction pattern contains the reflections used in Direct Methods. The remaining reflections were removed from the data set. Circles are drawn at 0.25 and 0.80 \AA^{-1} .

$10 < h^2 + k^2 < 90$ were kept in the final data set. Reflections with $h^2 + k^2 < 10$ were over-saturated and those with $h^2 + k^2 > 90$ corresponded to reflections belonging to higher order Laue zones (cf. Fig.3.13). Additionally, reflections corresponding to very weak intensities were reduced by 10% and their associated errors were increased by a factor of three. The final data set used in Direct Methods consisted of 94 reflections.

The diffraction pattern for the $(\sqrt{5} \times \sqrt{5})R26.6^\circ$ reconstruction shows that there are two domains of the surface structure on $\text{LaAlO}_3(001)$. The data mentioned in the previous paragraph pertains to the stronger domain of the surface unit cell. It should be noted however that Direct Methods was also carried out on the weaker domain (containing 88 independent reflections) and a weighed average of the stronger domain (D_1) and weaker one (D_2). The appropriate factors were determined through comparison of the stronger reflections in each data sets. The third data set (D_{AVG}) is given by

$$I^{h,k}[D_{\text{AVG}}] = (0.44)I^{h,k}[D_1] + (0.56)^{h,k}I[D_2] \quad (3.2)$$

$$E^{h,k}[D_{\text{AVG}}] = (0.23)E^{h,k}[D_1] + (0.77)^{h,k}E[D_2] \quad (3.3)$$

3.3 Structure Completion and Refinement

where $I^{h,k}$ and $E^{h,k}$ correspond to the intensity and error on each (h, k) reflection. Data set three (D_{AVG}) consisted of 81 independent reflections and was subsequently refined in $p2$ symmetry as well.

Direct Methods was then performed on each data set in the centered unit cell ($a=11.978 \text{ \AA}$, $\alpha = 89.89^\circ$) with various numbers of atoms. For example, two runs were performed for each data set with 15 atoms (3La, 3Al, 9O) and 75 (15La, 15Al, 45O) atoms. While stoichiometric ratios were used, deviations from the ideal bulk composition did not produce observable deviations in the solution maps. After running the genetic search, each data set produced a number of unique solutions (scattering potential maps) that yielded similar results. Therefore, the best data set, corresponding to the stronger domain (D_1), was used in all later refinements.

It is worth mentioning, that the primitive (non-centered) unit cell ($a=8.470 \text{ \AA}$, $\alpha = 90.00^\circ$) was also considered in the Direct Method analysis. Similar investigations were carried out for each domain as well (including both $p2$ and $p4$ Patterson plane group symmetries). The resulting scattering potential maps were consistent with those found for the non-primitive unit cell. The choice to use the centered cell was based on the problem of charge balance at the surface. Furthermore, this cell type aided in visualizing how the surface cell sits on the bulk and with site occupancy. Among the plausible solutions determined through Direct Methods, the best scattering potential map (the one used to obtain the structure solution) is shown in Fig. 3.14a. The Babinet solution, i.e. the calculated phases shifted by a factor of π [11], of this scattering potential map is shown in Fig. 3.14b. This solution was determined to be more stable than the original map, and therefore subsequent refinements were done on this genetic solution within the PEAKS program.

Through the use of difference maps, the projected structure was completed. Fig. 3.15 shows the structure solution map, and atomic model. The refinement of this structure against the experimental data allowed for the determination of in-plane atomic positions, i.e. x- and y-coordinates on the surface, with a $\chi^2 = 4.86$. The structure that was determined is rather simple and elegant, in that it is a lanthanum terminated surface with two La vacancies at the surface layer. This implies that the surface is non-stoichiometric or oxidized (oxygen rich) and lanthanum deficient. It is worth noting that no Al was found in the surface reconstruction, and the next section explains how the structure solution was determined. In particular, the analysis and choice of subsurface

3.3 Structure Completion and Refinement

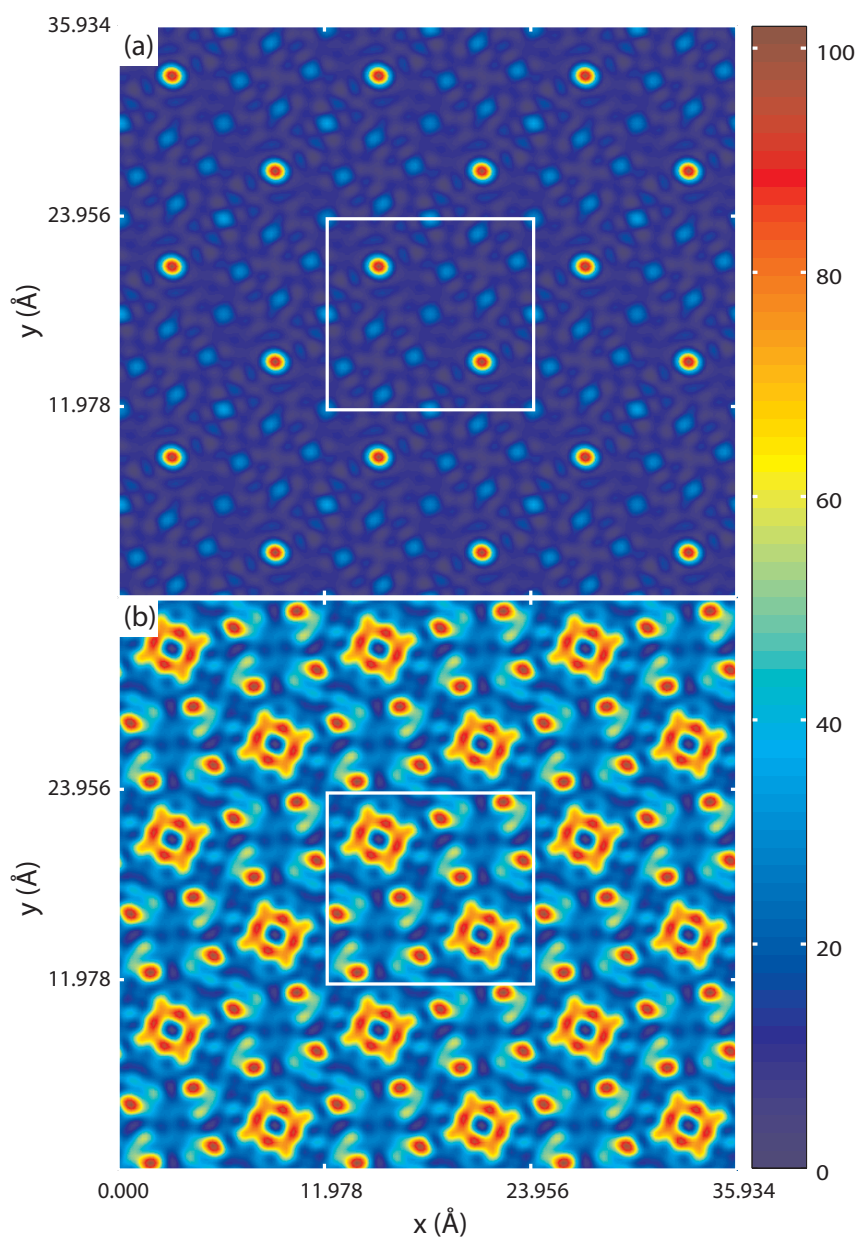


Figure 3.14: Direct Methods scattering potential map for (a) the LaAlO_3 ($\sqrt{5} \times \sqrt{5}$) $R26.6^\circ$ reconstructed surface, and (b) the Babinet solution, with the non-primitive surface unit cell ($a=11.978$ Å, $\alpha = 89.89^\circ$) drawn in (white). Regions of high potential in this projected scattering map correspond to likely locations for atoms.

3.3 Structure Completion and Refinement

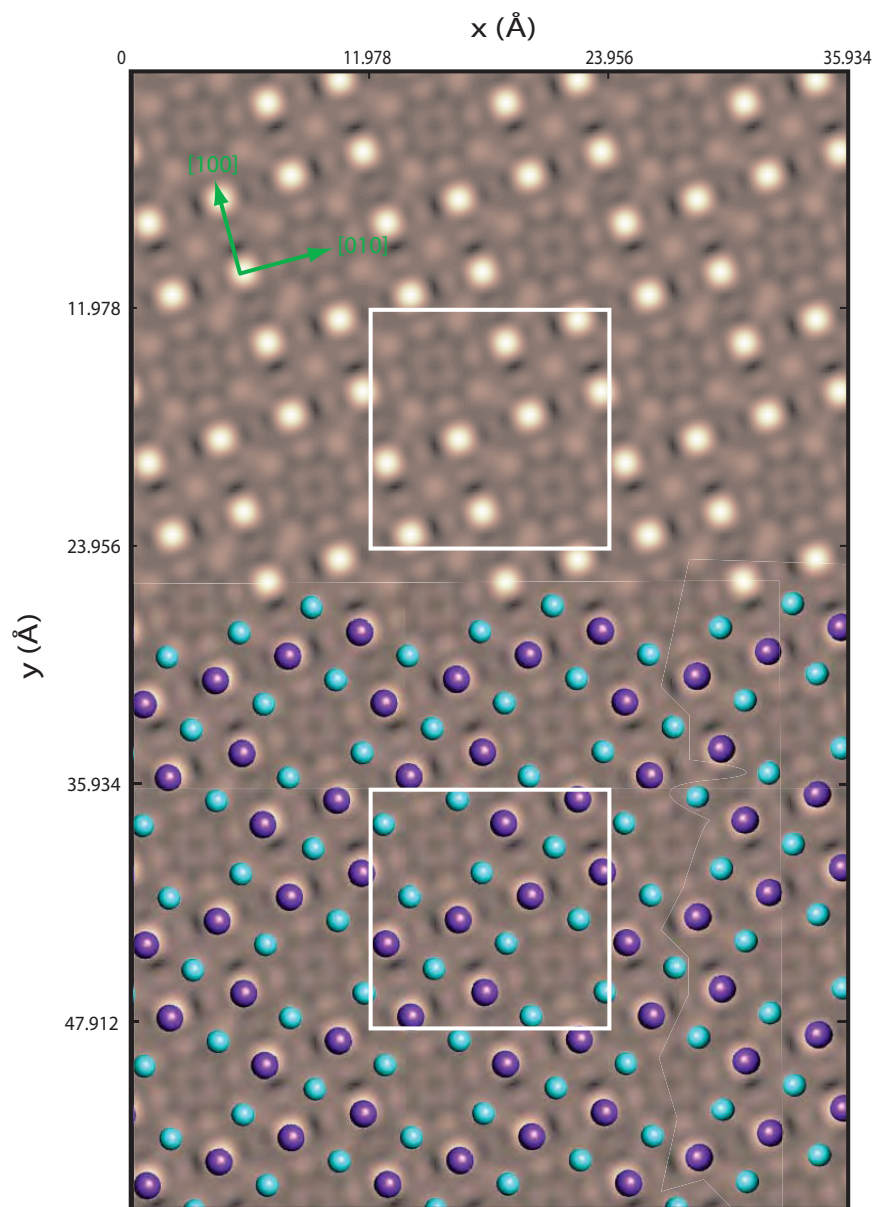


Figure 3.15: Structure solution map following refinements. The surface model has been overlaid. The bright spots correspond to La atoms (violet) and the weaker spots correspond to O atoms (cyan). The non-primitive surface unit cell ($a=11.978 \text{ Å}$, $\alpha = 89.89^\circ$) has also been drawn in (white). The orientation of the bulk relative to the surface reconstruction is denoted by the $[100]$ and $[010]$ axes (green).

3.3 Structure Completion and Refinement

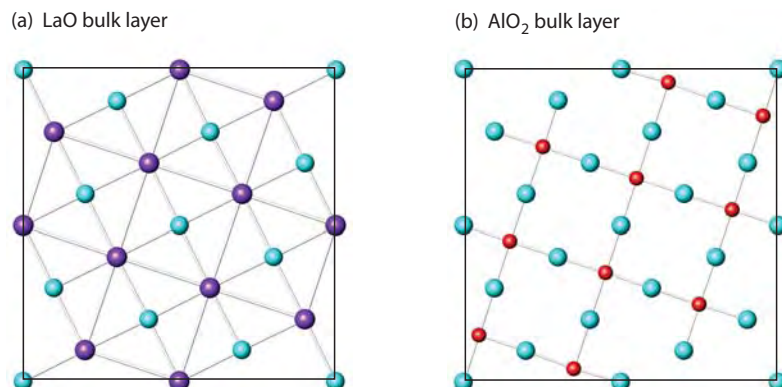


Figure 3.16: Bulk layers of (a) LaO and (b) AlO₂ with respect to the non-primitive surface unit cell ($a=11.978 \text{ \AA}$, $\alpha = 89.89^\circ$), with oxygen atoms at the origin (cyan) and lanthanum (violet) or aluminum (red) atoms, respectively.

layers in regards to how the surface unit cell bonds to the bulk reduces the possible surface models available. This surface-bulk registry is explored next and a more complete analysis of the solution is found in Sec. 3.3.2.

3.3.1 Bulk Registry

The structure completion was performed with the PEAKS program, which essentially reduces to a finding the appropriate atoms (at different sites) in order to satisfy the genetic scattering potential map. However, the code knows very little about the specific problem, in particular that the scattering species are atoms. It does not (directly) know about chemical constraints on atoms, such as bond distances, coordination or charge. For this reason, it was found useful to consider the various different bulk termination (subsurface) layers that would allow for the bonding of the surface structure.

The bulk material can be considered to terminate in either layers of LaO or AlO₂. Therefore the solution reduces to a set of six different subsurface layers, in actuality there are only two unique layers, centered about three possible origins each. Fig. 3.16 depicts the two layers relative to the non-primitive surface unit cell. With these two surfaces and the genetic solution, four unique stacking sequences (12 in all, if you include the various origins) must be considered. From the genetic solution and its Babinet, the surface layer consists of either two cation adatoms or two cation vacancies. At this point, it is clear that due to the size and orientation of the surface unit cell, simple stoichiometric changes

3.3 Structure Completion and Refinement

in the surface will not provide for charge compensation. Rather, a redistribution of the electronic structure (or change in valence) of near-surface layers (or atoms) must occur. While this may not be clear at the moment, it will be explored in Sec. 3.3.2. Additionally, the adatom or vacancy models will leave the surface either reduced (net charge of $+6e$ per non-primitive surface unit cell) or oxidized (net charge of $+4e$ per non-primitive surface unit cell). Therefore the set of possible solutions reduces to one of the following four cases:

1. La adatoms on a bulk AlO_2 layer,
2. La vacancies on a bulk AlO_2 layer,
3. Al adatoms on a bulk LaO layer, or
4. Al vacancies on a bulk LaO layer.

Using a good chemical intuition, four other options were eliminated—those which contained adatoms or vacancies of the same species on the same surface—since they made the least “sense.” While it is unlikely that the surface atoms do not arrange in this manner, it was nonetheless examined, because other perovskite materials have been observed with surface-rich reconstructions. In other words, they are bonded to the surface and composed of two of the same terminating layers [62, 63]. In either case, these models refined rather poorly (very large χ^2 values) and were disregarded.

Furthermore, options (1) and (3) were eliminated as possible surface models, because the cation adatom cases resulted in poor Fourier differences maps between the experimental and calculated diffraction patterns. For the case of scattering from a single atom, the diffraction pattern shows slowly decaying intensities in the reflections at increasing reciprocal space distances. While the adatom cases do create the appropriate diffractions spots, a majority of the experimentally observed structure in the diffraction patterns is lost. For this reason, only options (2) and (4) were determined to be feasible. With only two cases remaining, straightforward structure refinements using R-factors and χ^2 criterion led to the conclusion that La vacancies on an AlO_2 subsurface was superior to Al on a LaO subsurface layer. This model is rather simple in that the O atoms were found to be only minimally displaced from their bulk positions. Fig. 3.17 shows the surface structure model determined from Direct Methods, and how it fits onto the bulk material.

3.3 Structure Completion and Refinement

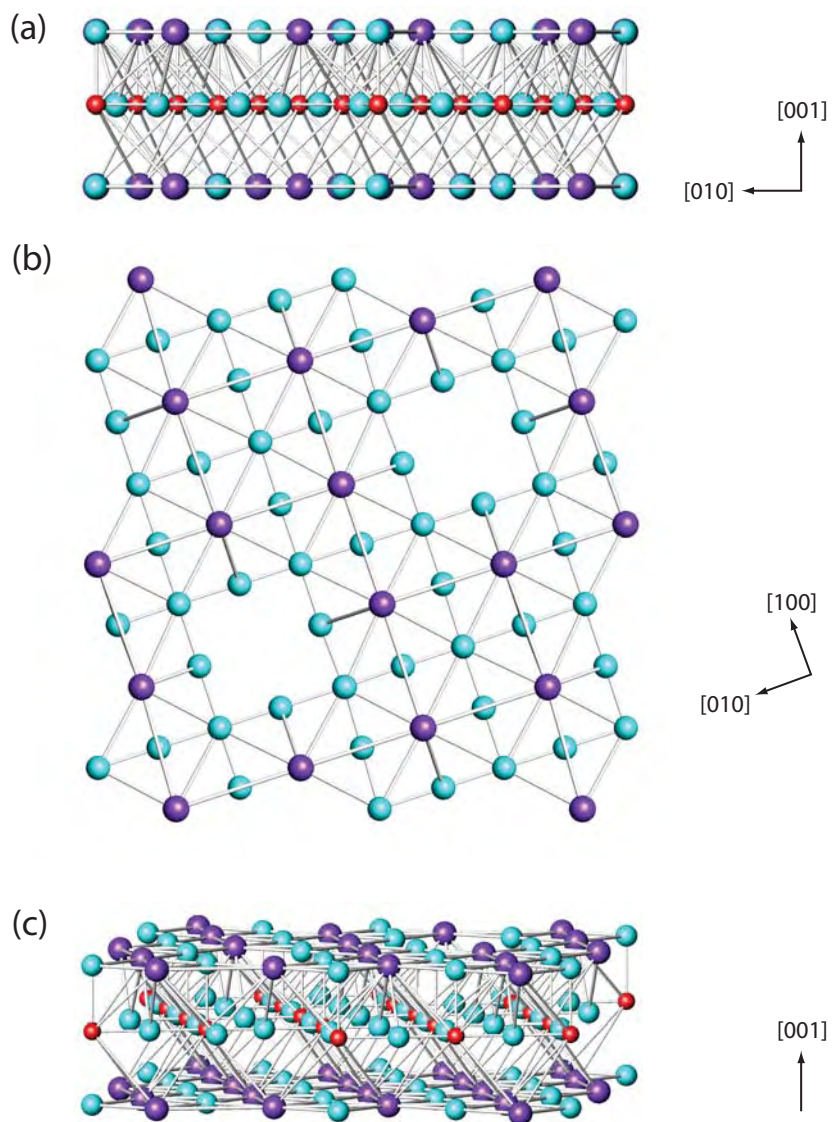


Figure 3.17: The $(\sqrt{5} \times \sqrt{5})R26.6^\circ$ structure solution from Direct Methods, the z-height positions are determined from typical bulk values and bond constraints. The La vacancy is discernible at the surface layer. The atoms are denoted as follows: oxygen (cyan), aluminum (red) and lanthanum (violet).

3.3 Structure Completion and Refinement

As a consequence of TED experiments, it is often times difficult to resolve atomic positions in the z -direction, since the scattering potential is a projection of the surface structure. However, the in-plane positions (x, y) can be found rather readily. The surface model shown in Fig. 3.17 is based on the refinements performed in the PEAKS program. The out-of-plane heights for the surface atoms in this illustration were set to be close to bulk positions and bond distances. As a result of the ambiguity of z -information, total energy electronic structure calculations were performed on this surface. These more accurate refinements and several conclusions are the topic of discussion in the next section.

3.3.2 Solution to the $(\sqrt{5} \times \sqrt{5})R26.6^\circ$ Surface

For convenience when discussing the atomic structure of the surface, the use of the non-primitive center unit will be abandoned. Rather, the primitive unit cell ($a=8.469 \text{ \AA}$, $\alpha = 90.00^\circ$) will be used through the remaining discussions. While the non-primitive unit cell was useful and for obtaining plausible surface models, the primitive cell is more appropriate for performing electronic structure calculations. Furthermore in the density functional theory (DFT) calculations, the equilibrium lattice parameter used for LaAlO_3 was about 0.67% larger than the literature value; this result however should have no effect on the structure conclusions.

The LaAlO_3 surface structure was geometry optimized using a three-dimensional periodic DFT surface slab model of 7 layers (81 atoms). This type of structure relaxation allows for the determination of the out of plane (and refinement of the in-plane) positions. The surface slabs were separated by a slab of vacuum of at least 6 \AA in thickness. The calculations were performed using the *ab initio* full-potential all electron (linearized-)augmented- plane wave + local orbitals (L/APW+lo) method as implemented in WIEN2K [64, 65]. The GGA potential approximation [66, 67] was used to obtain the fully relaxed positions. During the geometry optimization, atoms in the first three surface layers were relaxed, while the atoms in the remaining layer were fixed at their bulk positions. The atomic sphere radii were chosen to be 1.75, 1.75 and 2.33 bohr for O, Al and La, respectively.

3.3.2.1 Structural Refinement

The experimentally determined atomic positions for the surface atoms were used as the initial starting point for the DFT refinement. The refinement then

3.3 Structure Completion and Refinement

perturbed the atomic positions of the atoms until the calculated forces vanished (converged to a standard cutoff value). The results of the top 4 layers are listed in Table 3.2. Top and side views of the relaxed DFT structures are shown in Fig. 3.18.

It is clear that the experimental x- and y-positions agree well with theory. Although, it does appear that the deviations in the oxygen positions were greater than that of either cation. As noted, the theoretical calculations allow for the determination of the z-position for each atom. From Table 3.2, the experimental values are found to agree well with the calculations, which suggests that the surface retains almost bulk bond distance lengths. This in fact can also be seen from the deviation between the DFT calculated and bulk z-heights. Here, the layer separation was taken to be 1.911 Å (or 0.107 in fractional units). It is evident that all surface and subsurface layers retain most of their bulk spacings. However, the surface (layer 1) and layer 2 are shown to be rather ruffled (cf. Fig. 3.18). In particular, the La atom at the surface (La3) is pulled into the bulk by approximately 0.200 Å while the oxygens at the surface are displaced away from the bulk. Moreover, in-plane at the surface, the oxygen atoms are pulled away from the vacancy by the coordinating lanthanum atoms. This effect results in the misalignment of the oxygen rows at the surface. In layer 2, the oxygen atom (O6) at the edge on the unit cell is substantially pulled into the bulk, while the lanthanum (La12) in layer 3 is displaced toward the surface.

The AlO_6 octahedra at the surface are tilted in order to support the La vacancy reconstruction (cf. Fig. 3.19). In the bulk material this tilt angle is 5.15° while the surface octahedra are tilted approximately four times their typically bulk value (19.10°). This tilt angle was found by evaluating the analytical tilt expression for perovskites of $R\bar{3}c$ space group based on the fractional position of surface oxygens [68]. The octahedra formed by oxygens at the corners of the unit cell (O1), do retain their bulk tilt factors. The increased distortion in the tilt angle also modifies the bond length in the surface atoms, e.g. between atoms O2 and La3 (2.72 Å) compared to a bulk distance of 2.68 Å.

3.3.2.2 Charge Analysis

Initial investigation in the charge transfer of the reconstructions was performed to characterize the nature of the chemical bonding, and determine possible electronic structure redistributions. While the charge on the atoms in a solid cannot be uniquely partitioned (the charge density is a continuous field), there

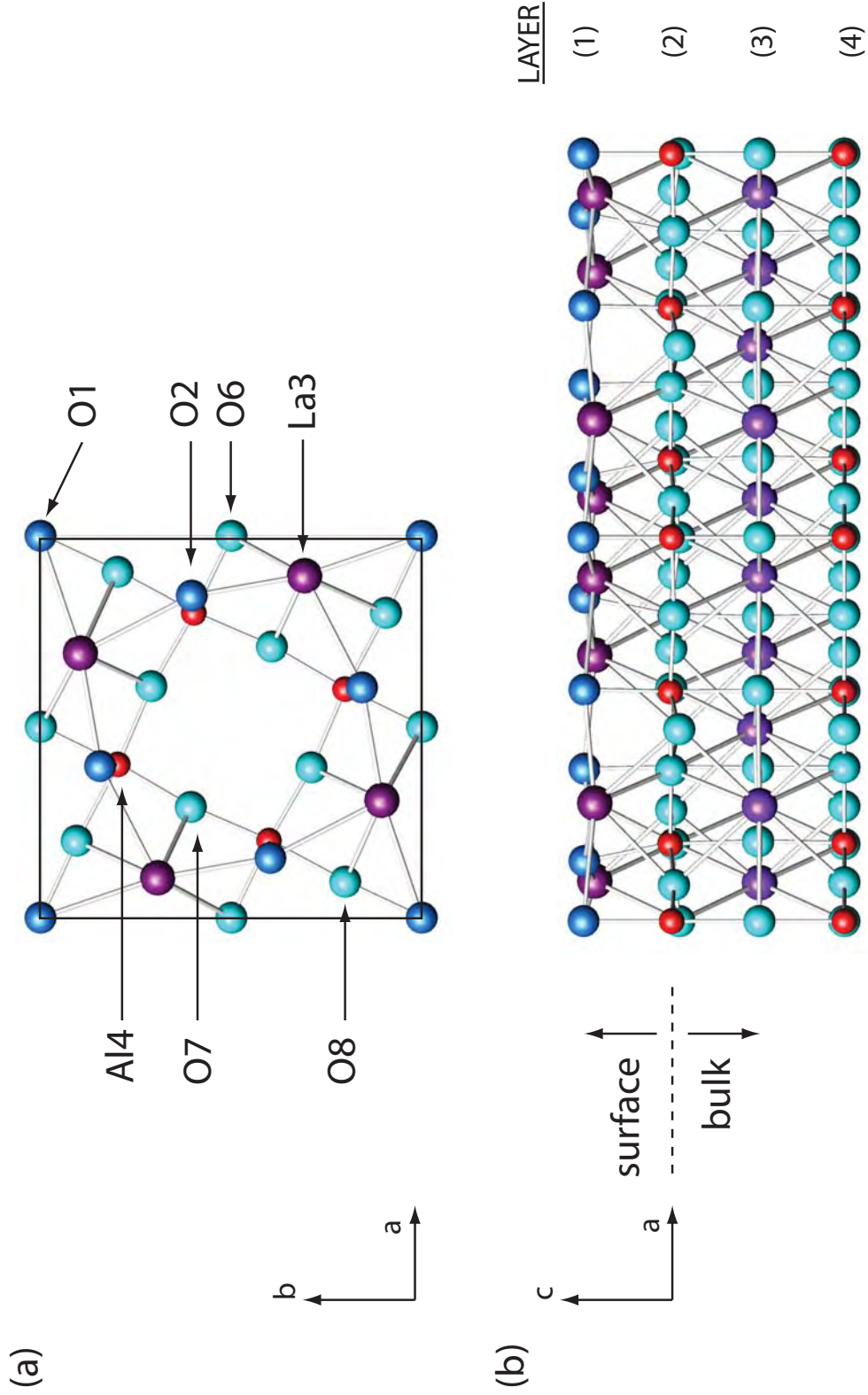


Figure 3.18: DFT solution of the $(\sqrt{5} \times \sqrt{5})R26.6^\circ$ surface structure: (a) top view with the surface unit cell outlined in black ($a=8.537 \text{ \AA}$, $\alpha = 90.00^\circ$), and (b) sideview. Atoms O1, O2 (blue) and La3 (magenta) are in the surface layer, while Al4, O6, O7 and O8 are in the second layer.

3.3 Structure Completion and Refinement

Layer ^d	Atom	Experiment										z _{DFT} - z _{Bulk} (Å)
		x	y	z	x	y	z	x	y	z	z (Å)	
1 (surface)	O1	0	0	0.321	0	0	0.324	5.787				+0.056
	O2	0.197	0.602	0.321	0.157	0.603	0.323	5.768				+0.037
	La3	0.697	0.102	0.321	0.693	0.105	0.311	5.538				-0.194
2 (subsurface)	Al4	0.197	0.602	0.214	0.202	0.599	0.217	3.863				+0.042
	Al5	0	0	0.214	0	0	0.215	3.830				+0.009
	O6	0	1/2	0.214	0	1/2	0.205	3.663				-0.158
3 (subsurface)	O7	0.299	0.400	0.214	0.290	0.394	0.215	3.841				+0.020
	O8	0.799	0.900	0.214	0.798	0.906	0.212	3.780				-0.041
	O9	0.197	0.602	0.107	0.208	0.600	0.107	1.915				+0.000
4 (bulk)	O10	0	0	0.107	0	0	0.106	1.887				-0.023
	La11	0.697	0.102	0.107	0.699	0.100	0.106	1.882				-0.028
	La12	1/2	1/2	0.107	1/2	1/2	0.112	1.989				+0.079
4 (bulk)	Al13	0.197	0.602	0	0.204	0.600	0	0				n/a
	Al14 [†]	0	0	0	0	0	0	0				n/a
	O15	0	1/2	0	0	1/2	0	0				n/a
	O16	0.299	0.400	0	0.299	0.401	0	0				n/a
	O17	0.799	0.900	0	0.799	0.899	0	0				n/a

^dIn the table, x - and y -coordinates are given as fractional coordinates of the square surface cell ($a=8.526$ Å). The z -coordinate (in Å) is given with respect to the bulk layer of the slab model; the atom marked with †, serves as that reference. Positive deviations indicate a displacement away from the bulk, while negative indicate a displacement into the bulk

Table 3.2: Experimental and DFT atom positions for the $(\sqrt{5} \times \sqrt{5})R26.6^\circ$ reconstruction.

3.3 Structure Completion and Refinement

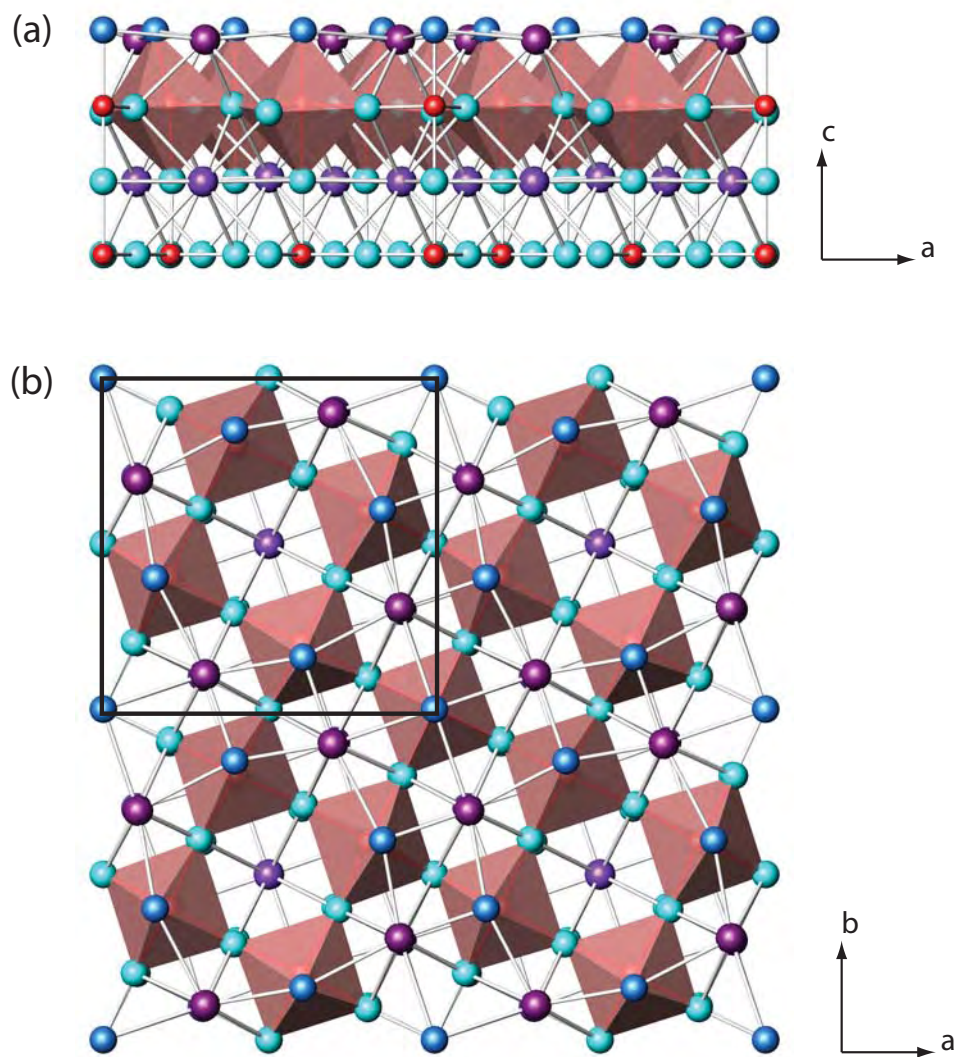


Figure 3.19: DFT solution of the $(\sqrt{5} \times \sqrt{5})R26.6^\circ$ surface structure: (a) sideview, and (b) top view with the surface unit cell outlined in black ($a=8.537 \text{ \AA}$, $\alpha = 90.00^\circ$). The AlO₆ octahedra have been shaded and the large distortion in the first surface layer is apparent. Surface lanthanum atoms are colored magenta, and surface oxygen atoms are blue.

3.3 Structure Completion and Refinement

Layer	Atom	Q^{AIM}	Excess
1 (surface)	O1	-1.477	0.06
	O2	-1.436	0.10
	La3	2.038	0.03
2 (subsurface)	Al4	2.550	0.00
	Al5	2.540	0.00
	O6	-1.492	0.05
	O7	-1.525	0.01
	O8	-1.515	0.02
Bulk	Al	2.550	
	La	2.067	
	O	-1.539	

Table 3.3: Bader’s AIM analysis of the partial atomic charges for the surface atoms of the $(\sqrt{5} \times \sqrt{5})R26.6^\circ$ surface reconstruction.

are several theoretical models which allow for an evaluation of the electron density. While these are not *real* charges on the atoms, they are a good estimate of the relative valency with respect to one another. In particular, Bader’s “Atom-in-Molecule” (AIM) method was evaluated for this reconstruction [69]. This method partitions the space into non-overlapping regions, each of which contains an atomic nucleus, known as a zero-flux surface. The AIM analysis was carried out using the charge density calculated from an all-electron method in WIEN2K. The advantage of using the AIM analysis over other models (e.g. Mulliken’s) [70] is due to the way in which AIM charges are uniquely defined for a given charge density. Table 3.3 lists the charges calculated for the various layers in the slab model.

Values for the third layer have been left out of Table 3.3, but were found to be very close to the bulk calculated values. In the surface and subsurface layer (2), the cations La3, Al4 and Al5 do not vary significantly from the bulk. However, for the oxygen atoms in the surface layer (O1 and O2) there is considerable deviation. As a result of the reduced charge on the surface oxygen, it is clear that an electron hole is localized at the near surface layers (between layers 1 and 2). The presence of this hole would allow for charge passivation of the surface layer, and quench the surface dipole moment. Further topological analysis, charge density maps, and density of states calculations are required in order to better quantify these results.

3.3 Structure Completion and Refinement

What is interesting for these studies is that charge compensation is not necessarily accommodated by stoichiometry changes. Rather, the electronic structure at the surface of a material is radically different than the bulk. If this variation is large enough at the surface, it may provide the driving force necessary for structural reordering. While this is probably not the only factor driving a surface to reconstruct, it nonetheless, must be considered just as important. Moreover, typical Ewald sums and electron counting models should not limit the set of feasible surface structures. While these methods are good at predicting which stoichiometries may exist at the surface, they do not allow for charge defects in (or at) the surface. For this reason, it is important to consider the presence of an electron or hole at interfaces for certain materials.

CHAPTER 4

Conclusions and Suggestions for Future Work

This work has begun the investigation into a new mixed metal oxide system, LaAlO_3 . Through various anneal treatments in air, it was found that the (001) surface first orders ($800\text{-}1100^\circ$) and then reconstructs into a $(\sqrt{5} \times \sqrt{5})R26.6^\circ$ surface (over $1100\text{-}1500^\circ$). The surface is characterized by faceting along the $\langle 100 \rangle$ and possesses subsurface voids. The reconstructed surface structure is rather elegant in that it is simply lanthanum deficient: owing to one lanthanum vacancy per surface unit cell. The oxygens in the first and third layers are slightly displaced from their nominal bulk positions, thereby forming distorted octahedra with the second layer aluminum atom. Furthermore, the electronic structure of the near-surface layers was modeled with standard density functional theory (DFT) in order to investigate charge transfer and charge defects. From a preliminary analysis, it appears that an electron hole is localized at the first surface layer due to the reduced charge on oxygen atoms at the surface. This charge defect may provide sufficient charge balance of the layers and reduce the net dipole at the surface.

While this study has enhanced our understanding of surface dynamics on polar oxide materials, much work remains to be done on improving our knowledge of what drives the surface to reconstruct. For example, further electronic structure calculations, along with charge density maps, will enable us to determine how the covalency in the material changes at the surface. Since the unreconstructed surface has a large free energy associated with it, the need for reconstruction could be driven by the surface strain energy, which upon reconstruction is relaxed by increased covalency between surface atoms.

In this study it has been proposed that the surface charge dipole is quenched by the formation of an electron hole in the near surface electron density. However, another feasible model would be the addition of a proton (e.g. a hydrogen atom) into the structure via free hydroxyl radicals or by the splitting of water at the surface. This alternative explanation requires investigation. It should be

considered both experimentally and modeled theoretically. Experiments (annealing) could be performed in controlled wet environments, either saturated or desaturated with water. Results of this experiments, and whether or not the surface reconstructs into $(\sqrt{5} \times \sqrt{5})R26.6^\circ$ would substantiate either argument (i.e. electron hole or proton model). Similarly, DFT calculations could determine the (relative) energies required to dissociate water into its native species at the surface. Comparison of this value with the surface strain energy may provide further evidence for either model. Additionally, the comparison of total energy for various hydrogen containing structures may suggest whether the hydrogen passivated surface is plausible. However, we can conclude that even for a relatively simple crystal system, oxide surfaces behave in drastically different ways than their bulk material: either through changes in atomic structure, chemical states, or in their electronic structure.

Furthermore, this study is just the beginning of a larger project on the LaAlO_3 material. For instance, different environmental conditions (temperatures, oxidizing or reducing atmospheres, UHV) may be explored to characterize the surface morphology. Furthermore, if the surface reconstructs to another known structure (on other perovskite materials), it may ultimately lead to a “recipe” for designing surfaces. In addition, various faces of LAO may be investigated, including the (110) and (111) since they are on average more interesting.

Finally, experiments to study the catalytic activity and selectivity of the surface would be desirable. If the surface proves to be active for a certain oxidation reaction, the structure of the surface could be related to its activity. This link would provide the ultimate structure-property relationship for the surface chemist. As a consequence, the engineering and design of new and more efficient catalysts would be attainable.

References

- [1] D.F. RUDD, S. FATHI-AFSHAR, A.A. TREVINO, AND M.A. STADTHERR. *Petrochemical Technology Assessment*. Wiley, New York, 1981. [2](#)
- [2] J.H. SINFELT. Influence of technology on catalytic science. *Ind. Eng. Chem. Fundam.*, **25**:2–9, 1986. [2](#)
- [3] F. BOZSO, G. ERTL, AND M. WEISS. Interaction of nitrogen with iron surfaces II: Fe(110). *Journal of Catalysis*, **50**(3):519–529, 1977. [3](#)
- [4] J.M. COWLEY. Electron microscopy of surface structures. *Progr. Surface Sci.*, **21**(3):209–250, 1986. [3](#)
- [5] J. VENABLES, D.J. SMITH, AND J.M. COWLEY. HREM, STEM, REM, SEM - and STM. *Surf. Sci.*, **181**:235–249, 1987.
- [6] G. JAYARAM AND L.D. MARKS. UHV-HREM and diffraction of surfaces. *Interface Sci.*, **2**:379–395, 1995.
- [7] A. SUBRAMANIAN AND L.D. MARKS. Surface crystallography via electron microscopy. *Ultramicroscopy*, **98**:151–157, 2004. [3](#), [26](#)
- [8] D. TABOR. *Gases, liquids, and solids: and other states of matter*. Cambridge University Press, London, 1991. [4](#)
- [9] W. SCHOMMERS AND P. VON BLANCKENHAGEN. *The Relevance of the Structure and Dynamics of Surfaces*, **41** of *Topics in Current Physics*, pages 1–16. Springer-Verlag, 1986. [4](#)
- [10] K. KERN. *Thermal roughening of surfaces: experimental aspects*, **7** of *The Chemical Physics of Solid Surfaces*, chapter 8. Elsevier, 1994. [4](#)

REFERENCES

- [11] L.D. MARKS, C. COLLAZO-DAVILLA, E. BENGU, E. LANDREE, D. GROZEA, C. LESLIE, AND W. SINKLER. Direct methods for surfaces. *Surf. Rev. Lett.*, **5**:1087–1106, 1998. [5](#), [6](#), [24](#), [25](#), [44](#)
- [12] P. XU, G. JAYARAM, AND L.D. MARKS. Cross-correlation method for intensity measurement of transmission electron-diffraction patterns. *Ultramicroscopy*, **53**:15–18, 1994. [23](#)
- [13] E. LANDREE, C. COLLAZO-DAVILLA, AND L.D. MARKS. Multi-solution genetic algorithm approach to surface structure determination using direct methods. *Acta Cryst.*, **B53**:916–922, 1997. [23](#), [26](#)
- [14] A. SUBRAMANIAN, L.D. MARKS, O. WARSCHKOW, AND D.E. ELLIS. Direct observation of charge transfer at a MgO (111) surface. *Phys. Rev. Lett.*, **92**(2):26101, 2004.
- [15] B. DENG AND L. D. MARKS. Theoretical structure factors for selected oxides and their effects in high-resolution electron-microscope (HREM) images. *Acta Crystallographica Section A*, **62**(3):208–216, May 2006. [6](#)
- [16] K. TAKAYANAGI, Y. TANISHIRO, M. TAKAHASHI, AND S. TAKAHASHI. Structural analysis of silicon(111)-7×7 by UHV-transmission electron diffraction and microscopy. *J. Vac. Sci. Technol. A*, **3**(ii):1502–1506, 1985. [6](#)
- [17] K. TAKAYANAGI, Y. TANISHIRO, M. TAKAHASHI, AND S. TAKAHASHI. Structure analysis of silicon (111)-7×7 reconstructed surface by transmission electron diffraction. *Surf. Sci.*, **164**(2):367–392, 1985. [6](#)
- [18] H. ROSE. Prospects for aberration-free electron microscopy. *Ultramicroscopy*, **103**:1–6, 2005. [6](#)
- [19] H A HAUPTMAN. The phase problem of x-ray crystallography. *Reports on Progress in Physics*, **54**(11):1427–1454, 1991. [6](#), [24](#)
- [20] P.B. HIRSH. *Electron Microscopy of Thin Crystals*. Washington, Butterworths, 1965. [7](#), [18](#)
- [21] L. REIMER. *Transmission Electron Microscopy*. Springer-Verlag, Telos, 1997.

REFERENCES

- [22] J.W. EDINGTON. *Practical Electron Microscopy in Materials Science*. Van Nostrand Reinhold Co., 1976. [7](#), [11](#), [18](#)
- [23] D.B. WILLIAMS AND C. BARRY CARTER. *Transmission Electron Microscopy: Diffraction*, **II**. Plenum Press, 1996. [15](#), [21](#), [22](#)
- [24] D.B. WILLIAMS AND C. BARRY CARTER. *Transmission Electron Microscopy: Imaging*, **III**. Plenum Press, 1996. [19](#)
- [25] A. CHIARAMONTI AND L.D. MARKS. In preparation, 2006. [20](#)
- [26] K. YAGI, K. TAKAYANAGI, K. KOBAYASHI, N. OSAKABE, Y. TANISHIRO, AND G. HOJO. Surface study by an UHV electron microscope. *Surf. Sci.*, **86**:174–181, 1979. [21](#)
- [27] J.F. VAN DER VEEN AND M.A. VAN HOVE. *The Structure of Surfaces II*. Springer Series in Surface Science II. Springer, Berlin, 1988. [21](#)
- [28] S.Y. TONG, M.A. VAN HOVE, K. TAKAYANAGI, AND X.D. XIE. *The Structure of Surfaces III*. Springer-Verlag, Berlin, 1991.
- [29] D.J. SMITH. *High-Resolution Electron Microscopy in Surface Science*, page 413. Springer, Springer-Berlin, 1986.
- [30] M.J. YACAMAN. *Electron microscopic methods*, page 183. Springer, Springer-Berlin, 1984. [21](#)
- [31] L.D. MARKS, P. XU, D.N. DUNN, AND J.P. ZHANG. Atomic imaging of surfaces in plan view. *Elec. Microscopy Soc. America*, **22**(3):65–69, 1992. [21](#)
- [32] R. KILAAS AND L.D. MARKS. EDM: Electron Direct Methods, 2004. [23](#)
- [33] G. GIACOVAZZO. *Direct Methods in Crystallography*. Plenum Press, New York, 1980. [24](#)
- [34] G. BRICOGNE. Maximum entropy and the foundations of direct methods. *Acta Crystallographica Section A*, **40**(4):410–445, Jul 1984.
- [35] M. M. WOOLFSON. Direct methods – from birth to maturity. *Acta Crystallographica Section A*, **43**(5):593–612, Sep 1987.

REFERENCES

- [36] C. J. GILMORE. Maximum Entropy and Bayesian Statistics in Crystallography: a Review of Practical Applications. *Acta Crystallographica Section A*, **52**(4):561–589, Jul 1996. [24](#)
- [37] P.L. COMBETTES. The convex feasibility problem in image recovery. *Advances in Imaging and Electron Physics*, **95**:155–270, 1996. [25](#)
- [38] R.W. GERCHBERG AND W.O. SAXTON. A practical algorithm for the determination of the phase from image and diffraction plane pictures. *Optik*, **35**:237–246, 1972. [26](#)
- [39] P.L. COMBETTES. *Advances in Imaging and Electron Physics*. New York Academic Press, New York, 1996. [26](#)
- [40] D.E. GOLDBERG. *Genetic Algorithms in search, optimization and machine learning*. Addison Wesley Longman, Inc., Massachusetts, 1997. [26](#)
- [41] J.M. COWLEY. *Diffraction Physics*. Elsevier, New York, 1984. [26](#)
- [42] R. BROWN, V. PENDRICK, D. KALOKITIS, AND B. H. T. CHAI. Low-loss substrate for microwave application of high-temperature superconductor films. *Applied Physics Letters*, **57**(13):1351–1353, 1990. [28](#)
- [43] T. STELZNER, H. SCHNEIDEWIND, AND G. BRUCHLOS. Superconducting Hg-Ba-Ca-Cu-O thin films on lanthanum aluminate and sapphire substrates. *IEEE Trans. Appl. Supercond.*, **13**(2):2766–2768, 2003. [28](#)
- [44] S. GELLER AND V.B. BALA. Crystallographic Studies of Perovskite-like Compounds. II. Rare Earth Aluminates. *Acta Cryst.*, **9**:1019–1025, 1956. [29](#)
- [45] G.W. BERKSTRESSER, A.J. VALENTINO, AND C.D. BRANDLE. Growth of single crystals of lanthanum aluminate. *J. Cryst. Growth*, **109**:467, 1991. [29](#)
- [46] H.D. MEGAW AND C.N.W. DARLINGTON. Geometrical and Structural Relations in the Rhombohedral Perovskites. *Acta Crystallographica Section A*, **31**(161):161–173, 1975. [29](#)
- [47] J. YAO, P.B. MERRILL, S.S. PERRY, D. MARTON, AND J.W. RABALAIS. Thermal stimulation of the surface termination of LaAlO₃ 100. *J. Chem. Phys.*, **108**(4):1644–1652, 1998. [30](#), [33](#), [34](#)

REFERENCES

- [48] R.J. FRANCIS, S.C. MOSS, AND A.J. JACOBSON. X-ray truncation rod analysis of the reversible temperature-dependent [001] surface structure of LaAlO_3 . *Phys. Rev. B*, **64**:235425–1, 2001. [33](#), [34](#)
- [49] H. KAWANOWA, H. OZAWA, M. OHTSUKI, Y. GOTOH, AND R. SOUDA. Structure analysis of LaAlO_3 (001) surfaces by low energy neutral scattering spectroscopy. *Surf. Sci.*, **506**:87–92, 2002. [33](#), [34](#), [35](#)
- [50] A. OHTOMO AND H. Y. HWANG. A high-mobility electron gas at the $\text{LaAlO}_3/\text{SrTiO}_3$ heterointerface. *Nature*, **427**(423):423–426, 2004. [30](#)
- [51] F. BERTAUT. The Electrostatic Term of the Surface Free Energy. *Compte Rendu (Chimie)*, **246**:3447–3450, 1958. [30](#)
- [52] P.W. TASKER. The stability of ionic crystal surfaces. *Journal of Physics C: Solid State Physics*, **12**(22):4977–4984, 1979. [30](#)
- [53] Z.L. WANG AND A.J. SHAPIRO. Studies of LaAlO_3 (100) surfaces using RHEED and REM I: twins, steps and dislocations. *Surf. Sci.*, **328**:159–169, 1995. [32](#), [34](#), [35](#)
- [54] J.P. JACOBS, M.A. SAN MIGUEL, AND L.J. ALVAREZ. Studies of LaAlO_3 001 surfaces by molecular dynamics simulations. *Journal of Molecular Structure (Theochem)*, **390**:193–198, 1997. [33](#), [34](#)
- [55] J.P. JACOBS, M.A. SAN MIGUEL, J.E. SÁNCHEZ-SÁNCHEZ, AND L.J. ALVAREZ. On the origin of the reconstruction of LaAlO_3 (001) surfaces. *Surface Science Letters*, **389**:L1147–L1152, 1997. [33](#), [34](#), [35](#)
- [56] D.A. SCHMIDT, T. OHTA, Q. YU, AND M.A. OLMSTEAD. Perovskite termination influence in oxide heteroepitaxy. *Journal of Applied Physics*, In press, 2006. [33](#), [34](#), [35](#)
- [57] P.A.W. VAN DER HEIDE AND J.W. RABALAIS. Photoelectron spectroscopic study of the temperature-dependent termination of the LaAlO_3 (100) surface. *Chemistry Physics Letters*, **297**(3-4):350–356, 1998. [33](#)
- [58] M.D. PASHLEY. Electron counting model and its application to island structures on molecular beam epitaxy grown GaAs (001) and ZnSe (001). *Phys. Rev. B*, **40**:10481–10487, 1989. [35](#)

REFERENCES

- [59] Z.L. WANG. Steps and facets on annealed LaAlO_3 (100) and (110) surfaces. *Surf. Sci.*, **360**:180–186, 1996. [35](#)
- [60] Z.L. WANG AND A.J. SHAPIRO. Studies of LaAlO_3 (100) surfaces using RHEED and REM II: (5×5) surface reconstruction. *Surf. Sci.*, **360**:180–186, 1996. [35](#)
- [61] N. ERDMAN AND L.D. MARKS. SrTiO_3 (001) surface structures under oxidizing conditions. *Surf. Sci.*, **526**:107–114, 2003. [41](#), [42](#)
- [62] N. ERDMAN, K.R. POEPELMEIER, M. ASTA, O. WARSCHKOW, D.E. ELLIS, AND L.D. MARKS. The Structure and Chemistry of the TiO_2 -rich surface of SrTiO_3 (001). *Nature*, **419**(55):55–57, 2002. [48](#)
- [63] N. ERDMAN, O. WARSCHKOW, M. ASTA, K.R. POEPELMEIER, D.E. ELLIS, AND L.D. MARKS. Surface Structures of SrTiO_3 (001): A TiO_2 -rich Reconstruction with a $c(4 \times 2)$ Unit Cell. *J. Am. Chem. Soc.*, **125**:10050–10056, 2003. [48](#)
- [64] P. BLAHA, K. SCHWARZ, P. SORANTIN, AND S. B. TRICKEY. Full-potential, linearized augmented plane wave programs for crystalline systems. *Computer Physics Communications*, **59**(2):399–415, 1990. [50](#)
- [65] P. BLAHA, K. SCHWARZ, G.K.H. MADSEN, D. KVASNICKA, AND J. LUITZ. *WIEN2k: An Augmented Plane Wave + Local Orbitals Program for Calculating Crystal Properties*. TU Wien, Vienna, Austria, 2001. [50](#)
- [66] JOHN P. PERDEW, KIERON BURKE, AND YUE WANG. Generalized gradient approximation for the exchange-correlation hole of a many-electron system. *Phys. Rev. B*, **54**(23):16533–16539, Dec 1996. [50](#)
- [67] JOHN P. PERDEW, J. A. CHEVARY, S. H. VOSKO, KOBLAR A. JACKSON, MARK R. PEDERSON, D. J. SINGH, AND CARLOS FIOHAIS. Atoms, molecules, solids, and surfaces: Applications of the generalized gradient approximation for exchange and correlation. *Phys. Rev. B*, **46**(11):6671–6687, Sep 1992. [50](#)
- [68] M. O'KEEFE AND B.G. HYDE. Some structures typologically related to cubic perovskite ($E2_1$), $\text{ReO}(\text{D}0_9)$ and Cu_3Au ($L1_2$). *Acta Crystallographica*, **B337**:3802–3813, 1997. [51](#)

REFERENCES

- [69] R.F.W. BADER. *Atoms in Molecules: a quantum theory*. Clarendon Press, Oxford, 1990. [55](#)
- [70] R. S. MULLIKEN. Electronic population analysis on lcao[single bond]molecular wave functions. i. *The Journal of Chemical Physics*, **23**(10):1833–1840, 1955. [55](#)